EUROPEAN ORGANIZATION FOR NUCLEAR RESEARCH

18 June 2000

A proposal for improving the thermal design of the ATLAS SCT end-caps

H. Becker[1] and J. Blocki[2]
University of Geneva, Geneva, Switzerland

B. van Eijk[3]
NIKHEF, Amsterdam, The Netherlands

and

T.O. Niinikoski
CERN, Geneva, Switzerland

Abstract

We present here an alternative thermal design for the wheels of the ATLAS SCT End-Caps. We achieve 30% savings on the overall thickness compared to the final baseline design presented in the Forward SCT Cooling Review (October 1999). Compared with the thickness contribution of the wiggly pipe system of the baseline design, the savings amount to about 75% of the cooling system components. Savings are mainly obtained by the efficient use of new materials and by eliminating the cooling points, blocks and pipes from the ends of the modules, opposite to the hybrid circuits. Further benefits are obtained by routing the cooling pipes circumferentially rather than radially through the cooling blocks, thus shortening the pipes by a factor of ~ 3. The simplicity of the proposed design offers improved reliability, and will reduce production time and cost.

This report includes extensive thermal calculations. Several techniques involved in using new materials to optimise the thermal performance are demonstrated. Based on our calculations and measurements, we present a complete wheel design. Extensive engineering drawings are publicly available and can be found on WWW. Thorough analyses show significant material savings can be achieved leading to a more robust and potentially better performing ATLAS tracker.

---

[1] On leave of absence, University of Saarbrücken, Germany

[2] On leave of absence, University of Cracow, Poland

[3] Also at the University of Twente, Enschede, The Netherlands

1. Introduction

1.1 Requirements

All subsystems of the ATLAS detector require active cooling because they are embedded in almost closed successive layers. Cooling by free convection of air alone is inefficient in removing the large amount of heat dissipated by the front-end readout electronics, cables and by the sensors. The cooling of the Semiconductor Tracker (SCT) has additional requirements:

- to ensure operation of the silicon detectors for 10 years in the LHC, and
- to give the lowest possible contribution to the multiple scattering, as requested also by the LHCC.

The first of these leads to requiring that the sensors be operated at or below the temperature of –7 °C because the evolution of the full depletion voltage of the sensors is slowest at this temperature. This is based on the finding that the beneficial and reverse annealing processes in the bulk silicon have different temperature dependencies. The optimum at the temperature of –7 °C, however, is very wide. Therefore, the life of the sensors is not greatly compromised even when operating at –20 °C. Moreover, this can be compensated by short annealing at a higher temperature which may take place during possible repair and maintenance periods.

Operation at temperatures above –7 °C may compromise the thermal stability of the lightweight modules because of the higher sensor current after heavy irradiation. The first requirement therefore leads to specifying the detector temperature at or below –7 °C. The thermal instability of the modules is due to the exponential increase of the leakage current of the sensors when their temperature increases. Thermal stability can easily be achieved by lowering the coolant temperature. This is possible by making the appropriate choice of two-phase coolant and by proper design of cooling pipes and blocks.

The second requirement follows directly from the specifications based on simulations of tracking accuracy, as well as the accuracy of the subsequent layers of calorimeters surrounding the SCT. The track deviation and energy loss due to multiple Coulomb scattering can be quantified by the material thickness measured in the terms of the parameter X_0 (radiation length). In the present baseline design of the End-Cap SCT the cooling pipes and blocks represent about 27% of the total disk thickness. Therefore, the LHCC reviewers of the ATLAS experiment recommended to the SCT and pixel communities to focus on the cooling systems of the ATLAS tracker, in view of achieving a significant reduction in the amount of material of the Inner Detector.

1.2 Guidelines based on SCT decisions

In their review in 1997, the LHCC suggested that evaporative cooling systems should be studied as an alternative to the planned cooling by a binary ice mixture. A conceptual design based on the two-

phase flow of C_3F_8 was presented in September 1997 [1]. Immediately, work was started for the experimental verification of the parameters and principles of the proposed Joule-Thomson cooling cycle. Additional coolants were also investigated, such as C_4F_{10}, which was the baseline refrigerant for the ATLAS Pixel detector, CF_3I, and mixtures of C_3F_8 and C_4F_{10}. After a series of tests and measurements [2] the SCT proposed C_3F_8 in the review of May 1999. The pixel community, due to pressure considerations, only changed formally to C_3F_8 in December 1999.

The above requirements and the decision of the IDSG, supplemented by decisions of the SCT management, result finally in the following guidelines for the design of the Fwd SCT cooling pipes and blocks:

1) The coolant is C_3F_8 and its temperature must be below –17 °C [1].
2) The temperature of the sensors must be below –7 °C, thermal run-away must be avoided after 10 years of operation in the LHC.
3) The disk thickness must be equal to or less than the present baseline design.
4) Solutions with hybrid and sensors thermally separated are preferred.
5) The module design should not deviate significantly from the present baseline design.
6) The number of disk pipe-work sectors must be equal to or less than 8/disk.

There may have been other specifications but in this work we have decided to adhere to those above to minimise the mass of the cooling pipes and blocks. Notably, we wish to choose the pipe diameter and geometry and the manifolding in such a way that engineering of the pipe connections and power tape layout would also result in maximal material savings.

Other parameters which have an impact on the thermal design and engineering, are the power dissipation in the readout electronics, optical components, sensors and power tapes. Their maximum characteristic values are given in table 1.

Source of dissipation	Power
Hybrid and optical components	7.2 W/module
Sensors at 0°C (∗)	240 μW/mm^2
Power tapes	0.45 W/m

Table 1: Maximum average power dissipation of the End-cap wheel heat sources, excluding the heat leak through the thermal isolation. (∗) See Eq. (1) in the text for the de-rating of the sensor power with temperature.

The power dissipation in the inner-ring sensors after 10 years of LHC operation varies as a function of the bulk silicon temperature by

---

1 This was announced in the Forward SCT Cooling Review on 12.10.1999.

$$\frac{\dot{Q}}{A_{Si}} = Q_0 \left(\frac{T}{T_0} \right)^2 \exp\left(-\frac{E_g}{2k} \left[\frac{1}{T} - \frac{1}{T_0} \right] \right) \quad (1)$$

where Q_0 = 240 μW/mm^2, E_g = 1.26 eV and T_0 = 273.15 K. This formula will be applied to estimate the thermal stability of the modules. It includes a safety factor of 1.5 in the fluence of the damaging particles, and a factor of about 3 in the silicon damage constant. Recent measurements of irradiated ATLAS SCT sensors indicate that the inner-ring module sensors dissipate only 117 μW/mm^2 at 0 °C after a radiation damage caused by a fluence of $3 * 10^{14}$ p/cm^2 [3]. This dose is equivalent to about 1.5 times one expects to receive during 10 years of LHC operation. The power density of Eq. (1) therefore includes an experimentally verified safety factor of 3 [3] compared with the present expectation for the inner-ring modules. This, and the additional safety factors included in the thermal stability evaluations, can lead to the use of an unnecessarily massive cooling system, notably when the modules are cooled with two cooling blocks and two pipes. For the middle-ring modules which receive a lower dose, the safety factor increases to 4 while for the outer ring an even higher factor can be derived.

The value of Q_0 evolves roughly linearly with the integrated luminosity of LHC. This also depends on the operating temperature and possible warm-up periods required for access and maintenance. The annealing of the radiation-induced defects in silicon will be influenced and both leakage currents and required operating voltage of the sensors are affected.

In our design, the power tapes on the disk have reduced lengths varying between 20 and 40 cm. Therefore, they will dissipate less than 0.2 W/module. Consequently, the maximum average power dissipation will be less than 8 W/module, the number we have used for calculating mass flow rates and cooling pipe diameters. Because of the geometry of the module layout on the wheels, the convectional heat load from the hybrid to the sensors varies from module to module. This is taken into account in the thermal modelling and stability criteria of the modules discussed in sections 4 and 5, but is of no relevance for the mass flow rates nor for the pressure drop calculations.

The robustness of the thermal design is ensured by assuming that all modules have the same power dissipation equal to the maximum value. Further checks will be made by reasonable variation of all relevant parameters in the numeric procedures to be described below. We believe that a sufficient safety can thus be obtained without resorting to the over-engineering which results from imposing large safety margins on all possible parameters of relevance in the design. In doing so, we avoid unnecessary cumulative effects (see Appendix III).

2. Cooling pipes

2.1 Circumferential pipe layout

We propose to design the system such that the modules can be operated safely with one circumferential cooling pipe passing through a ‘split’ cooling block, located at the junction of the hybrid and the end-tapped sensors. Details of the block design will be discussed in section 5. The modules are positioned on three concentric rings on the disks. The outer and inner ring modules are on one

side of the disk; the middle ring modules are on the opposite side. All 9 disks have the outer ring modules, whereas some disks have no inner and/or middle ring modules.

The approximate radii of the cooling pipes are given in table 2, together with the number of modules and maximum total power dissipation in each ring. The modules of each ring are cooled by two 'parallel' circumferential pipes forming an integral pipe ring, fed from the bottom and exhausted at the top of the wheel. The wheels with three rings of modules thus have 6 cooling pipes running from bottom to top. The mass flow in each parallel pipe is controlled by the expansion orifice or capillary, the relative discharge rates of which are measured at the time of fabrication of the pipe manifolds. The schematic flow diagram is shown in fig. 1. We note that the machining accuracy of the orifices should be ~ 5% or 5–10 μm, whereas it would be desirable to control the ratio of their diameters to 0.5% in order to achieve 1% accuracy in the relative mass flows. Laser drilling techniques can achieve these.

Ring	Radius (cm)	Number of modules	P_{max} (W)	Mass flow (g/s)	Orifice (mm)	x_{out} min. (at –17 °C)	x_{out} max. (at –27 °C)
Outer	43	52	208	2.70	0.389	0.84	0.87
Middle	47	40	160	2.10	0.343	0.83	0.86
Inner	34	40	160	2.10	0.343	0.83	0.86

Table 2: Circumference radii for pipes, total power dissipation per ring, mass flow in two parallel channels, orifice diameters, and output quality factors for the end-cap wheel cooling pipes. The quality factor after the expansion orifice is assumed to be x = 0.05 and the pressure difference is taken to be 5.0 bar.

The mass flow rate through the orifices is proportional to $\sqrt{\Delta p}$, the square root of the pressure differential across the expansion orifice (see Appendix for explanation). If the condenser operates with chilled water at 13 °C temperature, the condensation pressure can be varied between the saturation pressure 6.59 bar at about 15 °C and a higher pressure, which depends on the type of compressor used. Assuming that the compressor can reach 9 bar pressure, the mass flow rate can thus be boosted 21% higher than the values given in the table 2.

The sub-cooled liquid feed pipes arriving at the disks are thin-wall CuNi capillaries with 1.5 mm inner diameter and between 50 - 100 μm wall thickness.

The mismatch of the coefficient of thermal expansion (CTE) between the CuNi pipe and the disk may cause some deformation of the disk. If the disk is undeformable, a straight pipe would pull the blocks by a 70 N force at –30 °C pipe temperature. The resultant of the two almost opposite force vectors acting off the block is 11 N towards the centre of the disk for the inner and middle rings, and 8 N for the outer ring. This will cause a small tilt of the cooling blocks towards the centre. A CFC reinforcement bridge on top of the pipe can compensate the dilatation of the pipe and therefore the force acting on the blocks, if necessary.

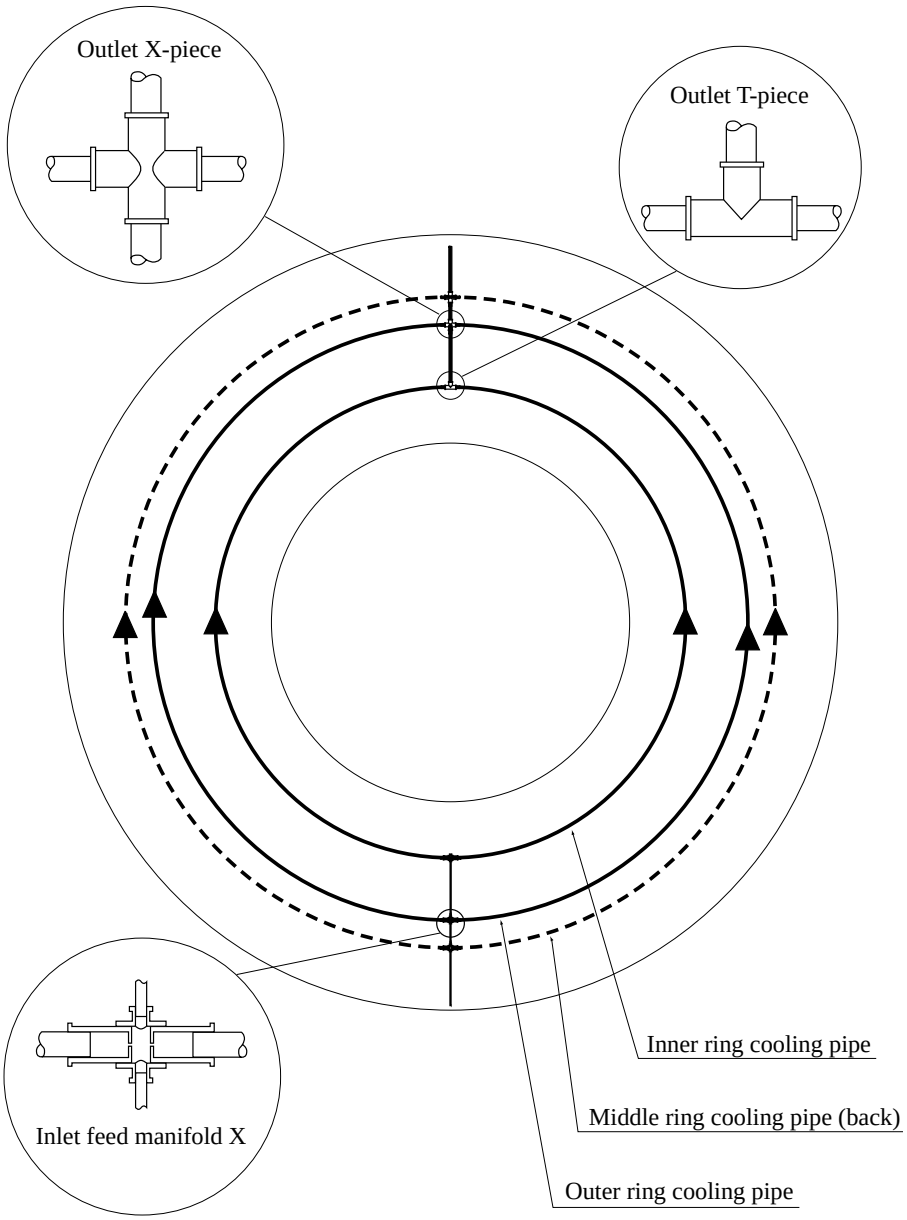

Figure 1: Schematic circumferential pipe layout showing six parallel cooling pipes running under the three concentric rings of modules (not shown). The dashed line shows the middle-ring-cooling pipe at the opposite side of the wheel. Details of the feed and exit pipe connections are also shown.

Our proposal to completely avoid the transfer of forces due to contraction and expansion of the cooling pipe due to temperature variation may involve the construction of composite cooling channels. NIKHEF has demonstrated that covering stainless steel pipes with carbon-fibre composites allows the tuning of the CTE of the channel. Several types of carbon fibres were applied and cured at room temperature. The measurements were calibrated by measuring a composite channel completely made out of carbon fibre (negative CTE) and a solid stainless steel tube. Moreover, repetitive thermal cycling shows no change in mechanical properties. The latter is not a surprise, since in carbon-fibre plies similar glue types bond the fibres. Similar glues have also been used in joining metallic and ceramic

pieces operating at temperatures below 1 K. These extremely demanding applications require absolute hermeticity under superfluid helium. Such vacuum feed-throughs have been thermally cycled hundreds of times between 1 K and 300 K, performing over more than 20 years without failure.

The ends of the semi-circular cooling pipes are mechanically linked in order not to cause asymmetric forces on the last and first cooling blocks in the chain. At the outlets and in the inlets these pieces form T-shaped or X-shaped pipe unions. The details of these pieces are shown in the inset of figure 1. Here, the design of the expansion orifices is shown in the inlet of the cooling pipes as well.

2.2 Pressure drop in the cooling pipes

The pressure drop in two-phase flow inside a heated tube arises from flow friction and from fluid dynamic effects, which are due to the increased momentum of the fluid (see Appendix). The sum of the two pressure gradients can be numerically integrated to yield the dynamic pressure at the locations of the cooling blocks. This dynamic pressure can be used for calculating the fluid temperature from the saturated vapour pressure equation.

Ring	T_{in} (°C)	p_{in} (bar)	Δp (bar)	ΔT (°C)
Outer	-27	1.54	0.16	2.6
Middle	-27	1.54	0.12	1.9
Inner	-27	1.54	0.09	1.4
Outer	-22	1.89	0.15	1.9
Middle	-22	1.89	0.10	1.4
Inner	-22	1.89	0.08	1.0
Outer	-17	2.30	0.13	1.4
Middle	-17	2.30	0.09	1.0
Inner	-17	2.30	0.07	0.8

Table 3: Pressure and temperature drops for cooling pipes with 3.5 mm inner diameter under the operating conditions defined in table 2, at three input temperatures. In practice, however, the output pressures and therefore the output temperatures are identical. Consequently, the input temperatures are higher by approximately ΔT given in the table. The error due to integrating the pressure drop from the beginning of the pipe till the end rather than the reverse, is less than 1% in ΔT.

We have estimated that our numeric procedures are accurate to better than 10% in the evaluation of the pressure drop based on the Chisholm equation. This is much better than the accuracy of the two-phase correlations, quoted to be about 40% for any fluid. No accurate experimental value exists

yet on the pressure drop for C_3F_8. Other methods of pressure drop evaluation give values slightly lower than those obtained with the Chisholm equation.

The pressure gradient in two-phase flow of C_3F_8 was evaluated at the two design mass flow rates for various pipe diameters, as a function of the molar fraction *x* of the vapour phase (this is commonly called the "quality factor" of the fluid), at three operating temperatures. The pressure gradient was integrated to yield the pressure at each cooling block. This pressure was then converted to fluid temperature using the equation for saturated vapour pressure. Using these results, presented in the Appendix, we have chosen the common pipe diameter of 3.5 mm so that under the worst conditions the maximum difference of input and output temperatures is 2.6 °C. This occurs in the outer ring cooling pipe at –27 °C coolant input temperature. In figure 2 we show the temperature distributions of the modules on the three rings for these three operating (input) temperatures of –27 °C, –22 °C, and –17 °C, and for the chosen pipe diameter. The corresponding pressure and temperature drops are summarised in table 3.

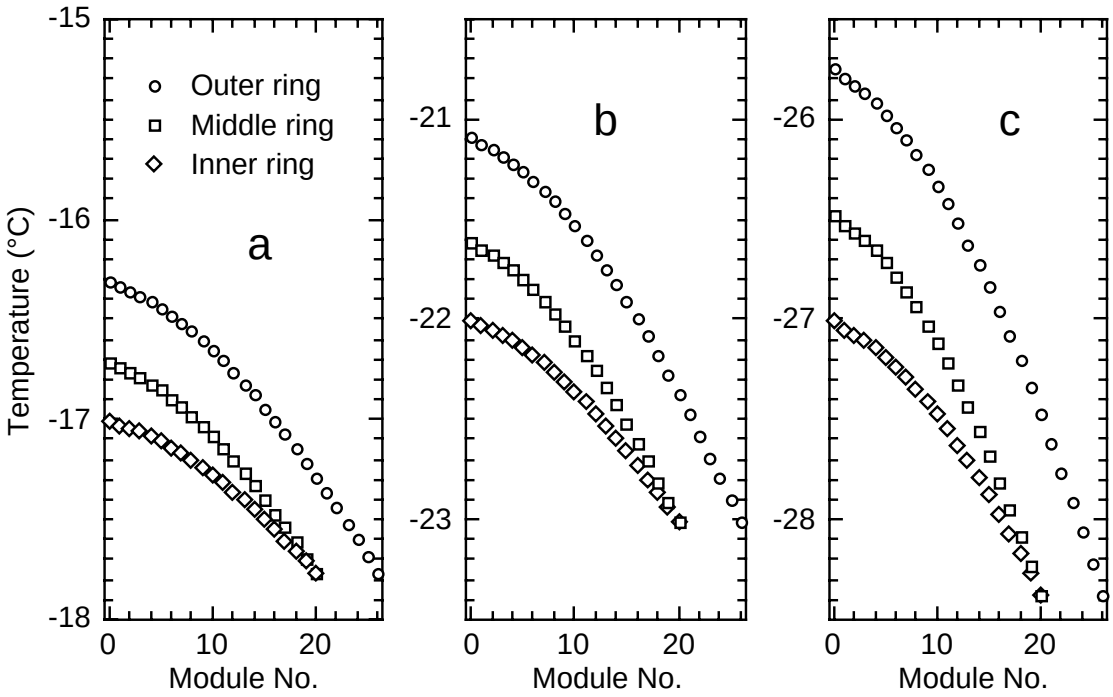

Figure 2: Coolant temperature distribution when operating around a) –17 °C, b) -22 °C and c) -27 °C at the cooling contacts of the modules of the three rings. The module numbers (1 to 20 or 26) are counted from the bottom to the top where the coolant pressures, and therefore temperatures, are identical. The temperatures at modules 0 (which do not exist) are those immediately after the expansion orifices.

The evaluation of the heat transfer coefficient described in section 3 was done at the fluid temperatures of –17 °C, –22 °C and –27 °C. As the coolant is not at a constant temperature in the cooling pipes, the heat transfer coefficient deviates slightly from the values given below. These

deviations are small in comparison with other sources of error, and we are therefore making the simplifying assumption of constant coolant temperature along the pipe in the evaluation of the temperature difference between the pipe wall and the coolant.

In the initial phase of LHC operation the coolant temperature distribution would be given by fig. 2a. After 10 years of operation, the temperature would have to be lowered closer to that given by fig. 2b, provided the sensor power density at 0 °C approaches 240 μW/mm^2. The operation under the conditions of fig. 2c ensure additional safety, which might be necessary to cover unforeseen failures such as frequent beam losses close to the detector at full luminosity. The maximum sensor power density at 0 °C tolerated in the scenario of fig. 2c is 400 μW/mm^2.

2.3 Cooling pipe walls and joining of pipes

The burst pressure of a thin-walled pipe of diameter *D* is

$$p_{burst} = \frac{t}{D}\frac{R}{\left(\mathrm{N\ mm^{-2}}\right)} \cdot 200\,\mathrm{bar} \qquad (2)$$

where *t* is the wall thickness and *R* is the rupture stress (= 570 N mm^{-2} for 70/30 CuNi). Assuming a wall thickness of 50 μm, a rupture pressure of 163 bar is obtained. For safe operation, a safety factor of 5 is applied; i.e. the maximum operating pressure should stay below 32 bar. The system can be easily designed so that the pressure cannot reach this value in any conditions.

In the case of stainless steel the rupture stress is about twice higher. The wall thickness can be reduced even below 50 μm. However, it is probably wise to stay above 20 μm thickness for the ease of handling of the pipes during manufacture and assembly.

The seamless cold-drawn capillary pipes are extremely homogeneous and therefore the risk of faults and leaks are no greater than in pipes with thicker wall.

The 70/30 CuNi has the advantages that it is extremely resistant against corrosion and can be joined by several soldering and brazing methods, including soft soldering with the rosin-core Pb/Sn solder which is used for electronics. This enables all-metal low-mass joints to be made at the time of the wheel assembly. The CuNi pipes can be soft soldered to carbon-carbon (C-C) composite cooling blocks after the blocks are coated by a thin layer (order of 10 μm) of Cu. This was tested using eutectic SnAg solder and solid-rosin flux and will be discussed in section 4.4. Brazing with an active alloy to bare C-C was tested and was found not recommendable because it requires a too high a temperature for the thin CuNi alloy pipes.

The lightweight tube fittings, T-pieces and distribution manifolds can be made of brass or CuNi. No corrosive flux is needed in the soft soldering process.

It should be stressed that soldering or brazing of thin-wall aluminium pipes is highly unreliable and can lead to rapid corrosion due to electrochemical processes.

Stainless steel, our second choice pipe material, needs to be vacuum brazed to C-C and pipe joints must be welded. Soft soldering is not recommended because the required acid fluid is extremely

corrosive. The vacuum brazing tests will be described in section 4.4.

Aluminium as a pipe material has the advantage that it has a large radiation length, about six times that of stainless steel. On the other hand, the poor corrosion resistance forces to use much thicker walls which in practice result in the same thickness contribution of the wheels. Moreover, the joining of thin-wall aluminium pipes can only be made by gluing which is highly unlikely to resist 10 years of thermal cycling in high-radiation environment. Equally important is that all plastics and epoxies have large variation in volume during prolonged exposure to fluorinated hydrocarbons; this will lead to leaks in the pipe joints after a few months of exposure.

Several steps remain in the further optimisation of both the construction of the cooling pipes and blocks, and in the assembly of the cooling structure to the disk. As an example, assume the C-C blocks soldered onto the bare (CuNi) pipe are both glued to the surface of the disk. During the same process step, pre-formed and pre-cured carbon-fibre covers can be mounted in between the blocks. The metal pipe will then be fully encapsulated in one single process step. In this scheme, mounting of the cooling pipes and blocks requires only moderate positioning precision. The precision locator hole for the module is machined into the block only after mounting.

As the distance between the neighbouring cooling block edges is small, and the pipe will be glued to the CFC skin in this gap, it may turn out unnecessary to provide additional stiffening structures on the bare pipe sections. Our planned thermal and mechanical tests will show the magnitude of the thermomechanical deformations on the disk. The test results will enable to design and to decide on the required compensating structures.

3. Heat transfer coefficient

3.1 Definition of the two-phase heat transfer coefficient

The heat transfer coefficient at an interface to the flow of boiling fluid is defined as

$$h = \frac{\dot{Q}/A_h}{\Delta T} \tag{3}$$

where $\dot{Q}/A_h$ is the heat flux from the heated pipe wall to the fluid, while ΔT is the difference between the wall temperature and the saturation temperature of the flowing fluid. The heat transfer to the flow of a boiling liquid is much higher than to the flow of sub-cooled fluid. This is due to the fact that two efficient mechanisms work in parallel in the former. These are the nucleate boiling on the pipe wall and the forced-convection heat transfer through the thin liquid film covering the tube wall in the annular flow regime. The mechanisms and the details on how the contributions are calculated are described in Appendix I.

Because heat transfer due to the nucleate boiling is highly non-linear, the overall heat transfer coefficient in two-phase flow is not a constant but depends on the heat flux and on the quality factor. It also depends on many fluid properties which change as a function of temperature. Therefore, the heat

transfer coefficient also depends to some extent on the saturation temperature and pressure. In the following subsections we shall demonstrate these dependencies and describe a procedure for deriving a single approximate formula, which yields the temperature difference as a function of all these three parameters.

3.2 Dependence on quality factor and temperature

The two-phase flow boiling heat transfer coefficient was determined from the dimensionless correlations at the fluid temperatures of –17 °C, –22 °C and –27 °C, at the heat flux of 4.5 W/cm^2. The results are plotted in figure 3 as a function of the quality factor *x*.

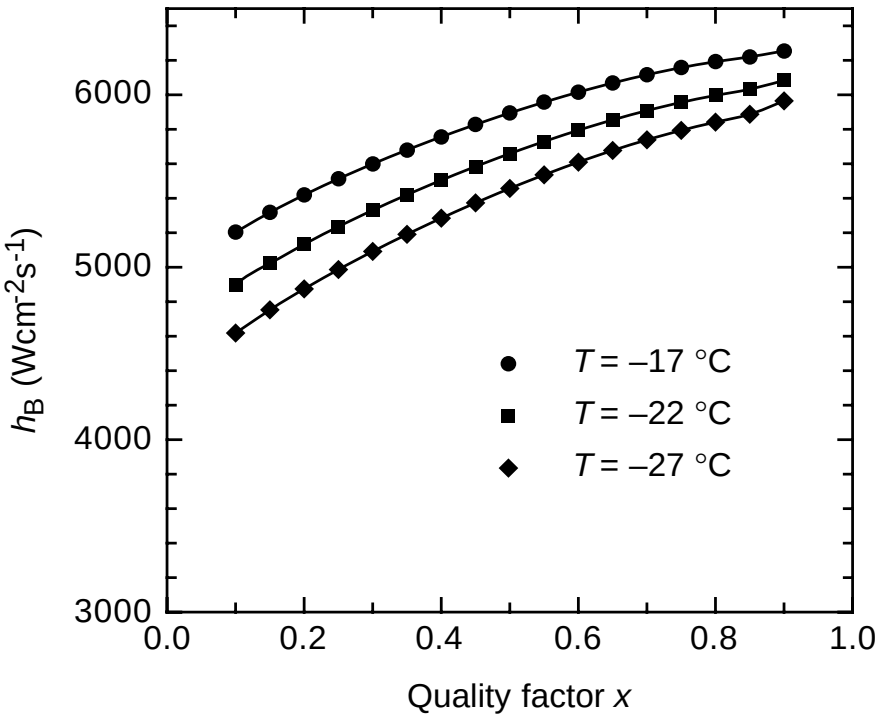

Figure 3: Dependence of the heat transfer coefficient on the quality factor x in the two-phase flow of the C_3F_8 coolant at the three temperatures chosen for the thermal design calculations. The pipe diameter is 3.5 mm and the mass flow rate is 2.7 g/s for the outer ring circumferential cooling pipe. The heat flux is 4.5 W/cm^2.

It can be seen that the coefficient is lower at low *x*, i.e. at the start of the cooling pipe. This leads to a larger temperature drop, which increases the temperature variation of the modules from the beginning of the pipe to the end.

At the shown temperatures this variation is not very dramatic and it may be quite well compensated by the larger convectional heat load to the silicon sensors on the upper half of the disks.

We note from figure 3 that the dependence of the heat transfer coefficient on the coolant

temperature is not very strong and is less than ±5% for the temperature deviations of ±5 °C from the value of –22 °C at which the subsequent evaluations are made.

3.3 Dependence on the heat flux at –22 °C coolant temperature

The non-linearity of the heat transfer is demonstrated in fig. 4 which shows the heat fluxes calculated from the dimensionless correlations, as discussed in the Appendix. The calculated values are fit by the approximate functions

$$\frac{\dot{Q}}{A} = h_B \Delta T = \Delta T\left[B_2 G(x) + B_1 S(x)\Delta T\right] \tag{4}$$

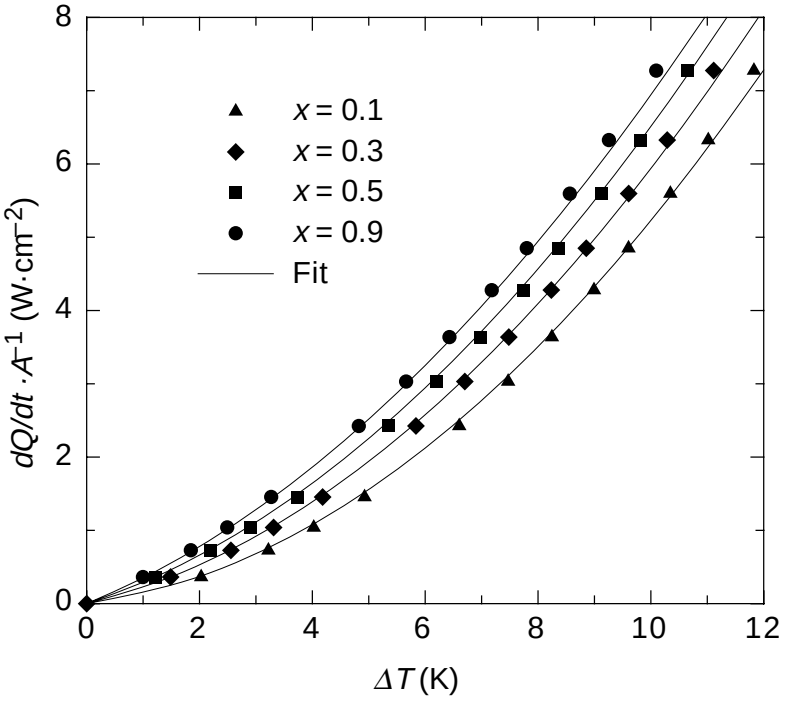

Figure 4: Heat flux as a function of temperature difference between the pipe wall and the C_3F_8 two-phase coolant at –22 °C temperature, with 2.7 g/s mass flow in the outer ring cooling pipe of 3.5 mm inner diameter, at different quality factors of the coolant. The points are calculated using the dimensionless correlations described in the Appendix. The lines represent fits to the calculated points using Eq. (4).

This is a simple second order equation, which can be inverted to give

$$\Delta T = \frac{B_2}{2B_1}\frac{G(x)}{S(x)}\left[\sqrt{\frac{4B_1 S(x)}{B_2^2 G^2(x)}\frac{\dot{Q}}{A}+1}-1\right] \tag{5}$$

The constants B_1 and B_2 and the functions $G(x)$ and $S(x)$ are given by Eqs. (A19) of the Appendix (at –22 °C coolant temperature).

Eq. (5) is practical for determining the temperature difference between the pipe wall and the coolant when performing thermal simulations of the modules and cooling blocks using finite-element analysis. It replaces the thermal resistors of the electrical analogue circuit by a 'thermal diode' behaviour. Such diode behaviour improves the thermal stability of the sensors, and reduces the module-to-module variation of temperature under different heat load conditions due to, for example, variations in the convectional heat load or in the sensor power dissipation in the different modules.

3.4 Experimental verification

Very little experimental data exists for the heat transfer coefficient in our proposed conditions for C_3F_8. We have therefore made a measurement using a split block; unfortunately there was very little time available to do the measurements with our set-up. Since the set-up was not sufficiently instrumented, we were not able to determine the quality factor of the fluid. Only a rough estimate from heat leaks into the various parts of the system could be obtained. The results are shown in fig. 5.

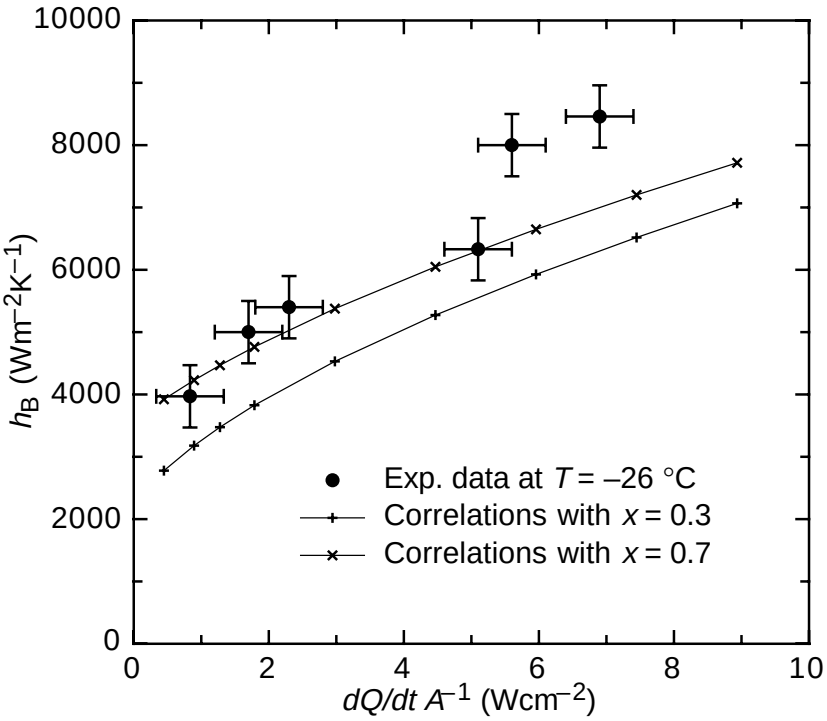

Figure 5: Comparison of the experimental data at -26 °C temperature for C_3F_8 using a split cooling block described in the text, with the heat transfer coefficient calculated using the method described in the text and in the Appendix. The mass flow was about 2 g/s and pipe diameter 2.85 mm. The quality factor was unknown and is expected to be ~ 0.5 ± 0.3.

At very high heat fluxes, allowed by the high heat transfer coefficient, the conductivity of the various materials of the block influence the temperature measured on top of the block. A correction was made for this and the vertical error bars reflect the size of this correction and the errors in the thermometry. The horizontal error bars result from the estimated errors in the contact surface between the pipe and the cooling block, from the estimated heat leak which was corrected, and from minor errors in the measured power dissipation.

The data are in fair agreement with the calculated HTC at x = 0.7; however, the quality factor is likely to be much lower because the block was mounted at the start of the cooling pipe. The calculated values are therefore underestimating the experimental HTC. On the other hand the dimensionless correlations, the reduction and suppression factors for the nucleate boiling and forced convection heat transfer, are known to result in no better than 40% accuracy in the calculated value for the different fluids. More accurate and systematic measurements of the heat transfer coefficient would therefore be required to fully detail the engineering design.

In view of the above, we have decided to use the calculated HTC rather than the measured values. This is conservative because the calculated values seem to be about 20% lower than experimentally obtained.

4. Cooling of the modules

4.1 Principle of split cooling block

There are two main heat sources to be considered. Firstly, the hybrid power $\dot{Q}_h$ is assumed to be constant with a maximum value of 7.2 W. Secondly, the sensors dissipate power, $\dot{Q}_s$, which is less than 1 W after full irradiation, while we introduced a safety factor of four at our proposed coolant temperature slightly below –22 C (see Eq. (1)).

Figure 6: Full solid model of a split cooling block. The largest area provides cooling for the hybrid (grey); the dark grey area cools the sensors. Details of the design are discussed in section 4.3.

The heat flux of both sources should be kept separated up to the sink, which is the coolant. Because $\dot{Q}_S$ is small, the temperature of the sensors will be close to the coolant temperature, which will ensure that $\dot{Q}_S$ remains small. The temperature of the hybrid is a less critical issue, but at high values there will be an increased heat transfer to the sensors by convection and radiation.

An effective separation of the two heat paths has to be introduced in the module itself, while good separation of the paths from the two separated cooling contacts down to the coolant is mandatory. These paths can be brought close together to form the 'split block'. Mechanical connections should have only very weak thermal links. A full solid model of a split block is presented in figure 6 (for details see section 4.3).

Furthermore, for the two heat paths we have conflicting requirements of a low contribution to multiple scattering and of supporting a high heat flux with low thermal gradient. Also the separation of the heat paths has to be achieved with a minimum of insulating material. To achieve both, proper materials have to be applied.

If both halves of the block have a sufficiently good thermal performance, or if the coolant temperature is sufficiently low, additional (second) cooling contacts for the sensors are not required and the second cooling circuit can be eliminated. In fact, the inner ring modules in the baseline design do not use such second cooling circuit.

4.2 Design of module

Modifications to the baseline module design are necessary, when one wants to maintain the coolant temperature at a relative high value. Several improvements have already been suggested. Changes are relatively small, since no modifications to the sensors can be made at this stage. Similarly, the hybrid design has progressed quite far already and major changes in the layout would require extensive debugging of the circuitry.

The crucial newly designed area is located around the cooling contact and is shown in figure 7. Firstly, the thermal separation between hybrid and sensors is improved by increasing the gap bridged by the quartz fan-ins from 2 to 5 mm. In addition, the connection pieces between the fan-ins and the sensors are also made of quartz rather than AlN. These components must provide a safe mechanical link, must be preferably made of a material with low heat conductivity and must have reduced size. The washer (with a precision hole) is modified so as to avoid any thermal bridge.

Secondly, the sensor heat path is improved by making the TPG strip wider (from 12 to 20 mm) and by reducing the AlN lamination at the end to a minimum. This ceramic piece, required for electrical isolation, needs only to cover the surface of the cooling block. We should stress that the BN-filler in the glue does not yield any relevant thermal advantage due to the large glue contact area between sensors and TPG. The filler would only complicate the module assembly.

Thirdly, the hybrid heat path is improved by increasing its contact area with the block, while decreasing the sensor-to-block contact area. This is justified since the new CFC baseboard has a

higher heat resistance perpendicular to the fibres and because a high power has to be transferred. The corresponding larger area of the hybrid, in contact via a thin layer of thermal grease with the cooling block, will help in reducing the temperature at the edges of the hybrid. For the contact area a sufficient pressure is obtained by a fixing nut and a shaped washer.

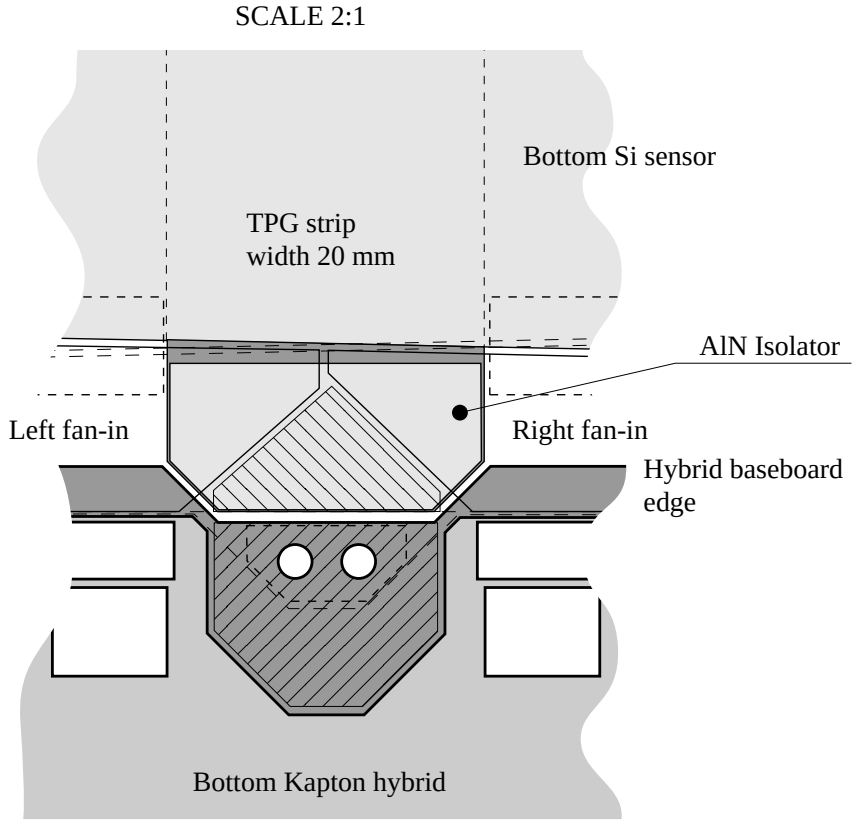

Figure 7: Modified thermal contact area of the outer ring module seen from the bottom. The areas in contact with the cooling block are hashed. The AlN isolator is partly covered by the bottom fan-ins that make the structure rigid; the top fan-in is one single piece and covers the TPG strip extension entirely. Similar changes are valid for the inner and middle ring modules.

These modifications will already result in a reduction of the module mass. Further reduction can be achieved by adopting the so-called box-design where the stiffness is given by the four sensors themselves, mechanically connected by sandwiched spacers as shown in figure 8. The shape of the TPG strip -without mechanical function- should be further optimised for heat transfer and mass reduction by FE simulations. Although this design might be inconvenient in some assembly methods, it

is perfectly compatible with that used by the CERN-Geneva Cluster. Moreover, this assembly procedure has achieved the best mechanical precision so far.

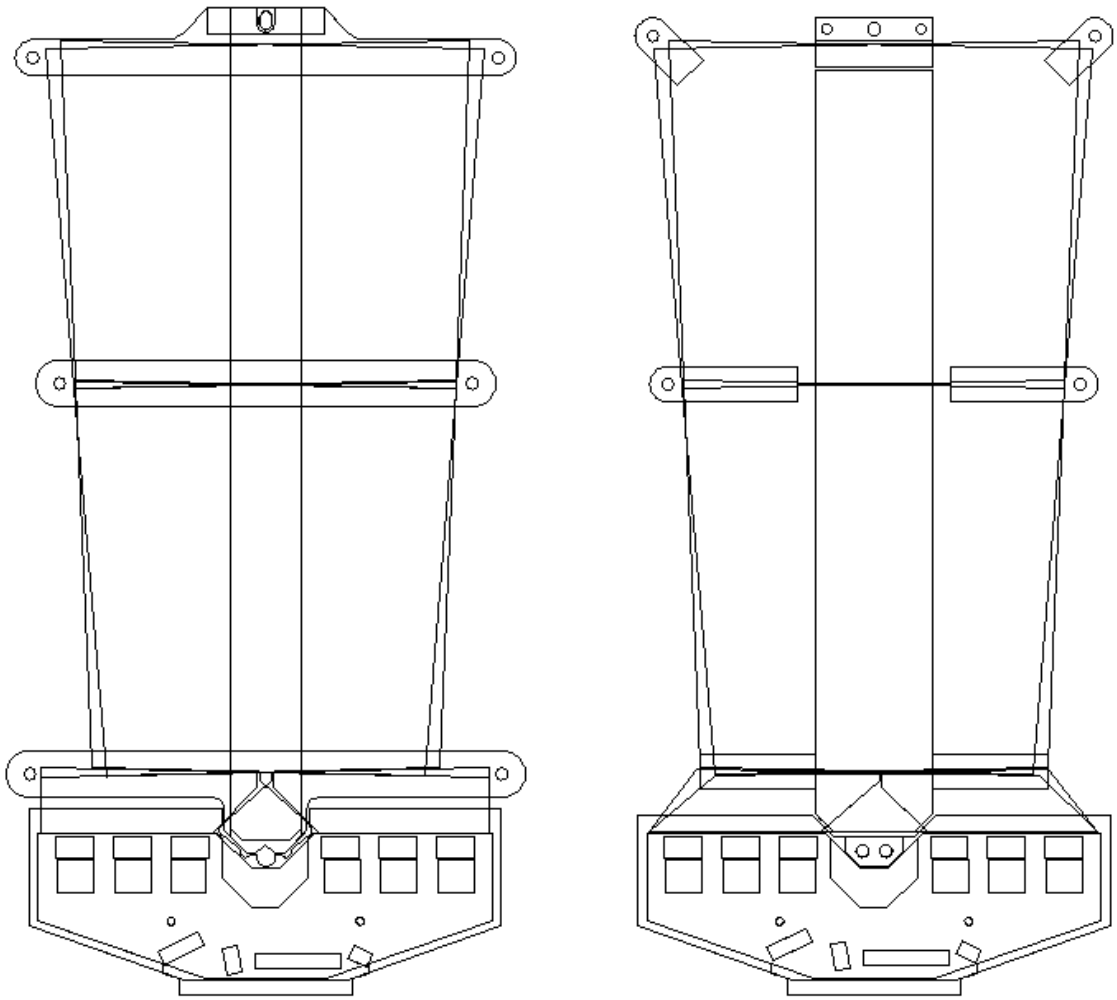

Figure 8: Modifications to the outer ring module (right), compared with the baseline design (left).

The spacers can be butt-joined to the TPG strip if an assembly method requires that the module spine forms one integrated part. The butt joints can be made by gluing and gluing thin Mylar strips over the joint areas in the same step can strengthen the joints. Besides the improved thermal performance, the benefits of our module design are (a mechanical prototype has been assembled and is shown in figure 9):

- Lower thermal stresses and distortions.
- Cost saving amounting to more than 400 kSF, which is 75% of the structural components, mainly by replacing the AlN cross-bars that require precision milling to the proper thickness.
- Material savings: the module thickness is reduced from 1.136%X_0 to 1.018%X_0 (~ 10%). This is equivalent to thinning the sensors from 300 µm to 250 µm.

- Eliminating the far-end cooling block allows replacing the extension of the spine by a small Al piece with a precision slot. Therefore, the total length of the module may be reduced.
- It is advantageous to use a 3-point fixation with two fixing points at the far-end of the module. This is to minimise possible tilt of the module due to the grease contact at the split block. In our scheme the location pin at the far end is captured in the precision slot of the Al piece, separated from the two fixing points with screws. The baseline design requires a mechanically less precise sliding-grease joint to connect to the second cooling circuit.
- The topside fan-in can be made of a single glass piece. This strengthens the TPG tongue underneath. It also reduces the risk of delaminating the AlN isolator glued under the tongue when extracting the module already fixed by thermal grease at the cooling block.
- On the Al washer, glued to the hybrid, a thread is foreseen for retracting the module from the grease contact using a simple tool. The tool can also be used for safe handling of the module.
- The modified hybrid contact area straightens the split in the block and simplifies the design/manufacture of the hybrid baseboard and of the block itself (see next section).

Figure 9: Mechanical prototype of the improved module design.

4.3 Design of split cooling block

In the module the thermal isolation between hybrid and sensors was achieved by using quartz in the fan-in area. High thermal conduction in the sensor and hybrid heat paths was obtained by using

TPG for the sensors and a CFC baseboard for the hybrid. In the cooling block the thermal isolation is achieved by the use of a thin-walled CuNi pipe as a mechanical connection between the two block halves, and good thermal conduction is achieved by using C-C composite as block material. The effective thermal fin length of the pipe wall is only 0.5 mm (see Appendix A.I.7), so that a gap of 1 mm is sufficient between the block halves.

The C-C composite has a radiation length X_0/ρ = 220 mm and thermal conductivity similar to Cu, 400 $Wm^{-1}K^{-1}$ in the good directions and 75 $Wm^{-1}K^{-1}$ in the third direction. The latter is still a reasonable value. This material is used in brake-disks of aeroplanes. The plane of better thermal conduction should be oriented so that a lowest possible contact surface temperature is obtained for each side of the block; this implies a different orientation in the two cases.

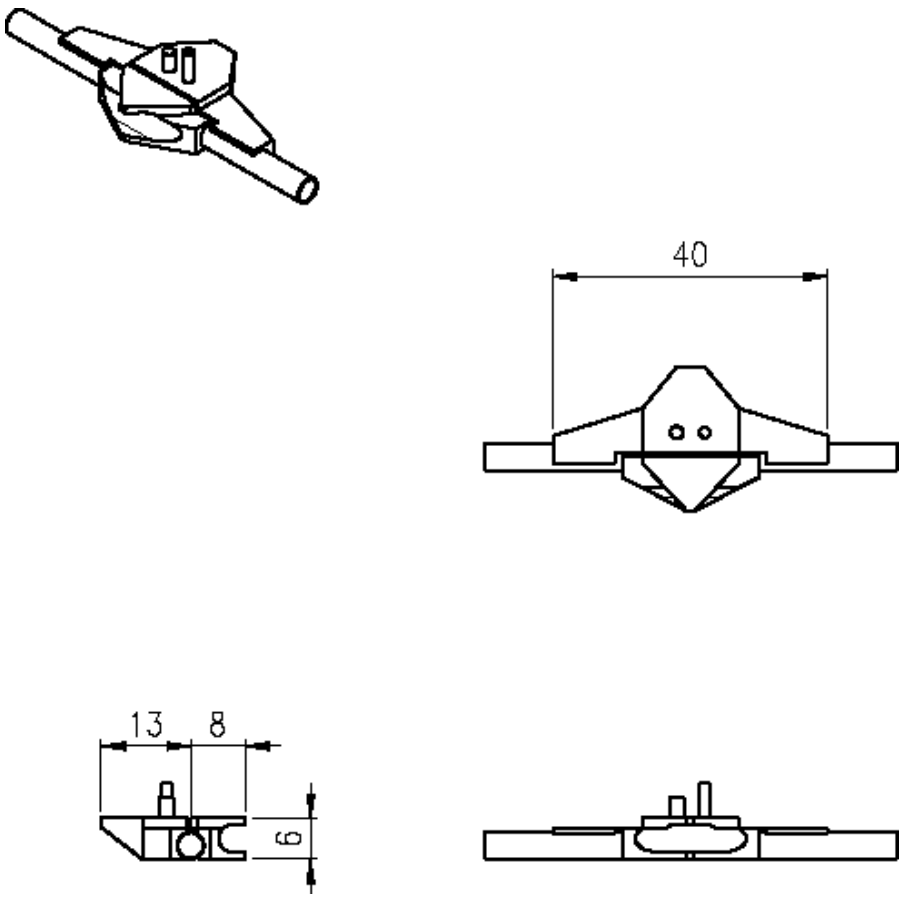

Figure 10: The mechanical design of the lower split cooling block. The cooling surface of the block cooling the top (staggered) modules is 4 mm higher. A 2 mm diameter dowel pin and M1.6 screw for locating and fixing the hybrid to the block are indicated as well. The outer pipe diameter is 3.6 mm.

The design of the split block, illustrated in figure 10, was driven to get sufficient thermal efficiency at a low material volume. The coolant contact surface areas on the hybrid and sensor sides of the cooling block must be dimensioned so that the sensor block will be always colder than the hybrid block. As the hybrid block always conducts about 7 W to the cooling pipe and the maximum power

from the sensors is limited to 1.75 W by the power supplies, a rough criterion for the ratio of the contact surfaces becomes

$$\frac{A_{hybrid}}{A_{sensors}} < \frac{\dot{Q}^{\max}_{hybrid}}{\dot{Q}^{\max}_{sensors}} = \frac{7}{1.75} = 4 \qquad (6)$$

This ensures that in all conditions the thermal splitting of the block helps in maintaining the thermal stability of the sensors. If this condition is violated, the sensor block would be hotter than the hybrid block before the maximum sensor power is reached, and therefore an unsplit block would better ensure thermal stability at the maximum power. In other words, an unsplit block would then enable stable operation at higher coolant temperatures than the split block would do.

Inclusion of the convective heat load from the hybrid to the sensors slightly lowers the ratio in expression (6). In our design the contact areas are 2 cm^2 for the hybrid and 1 cm^2 for the sensors respectively, satisfying the inequality.

The circumferential cooling pipe runs at the bottom of the block and is glued together with the blocks onto the disk (fig. 11). This provides cooling of the disk and reduces the heat transfer via convection and radiation to the sensors. The width of the block is enlarged to 40 mm to optimise the contact area (2 cm^2) between block and pipe. This is possible, because the power tapes in our design do not have to run between the blocks as in the baseline. Little space is needed between the blocks for bending the pipes to become circumferential. The ‘poor’ heat conducting direction of the C-C is chosen for the hybrid side to be downwards to the disk, for the sensor side along the pipe.

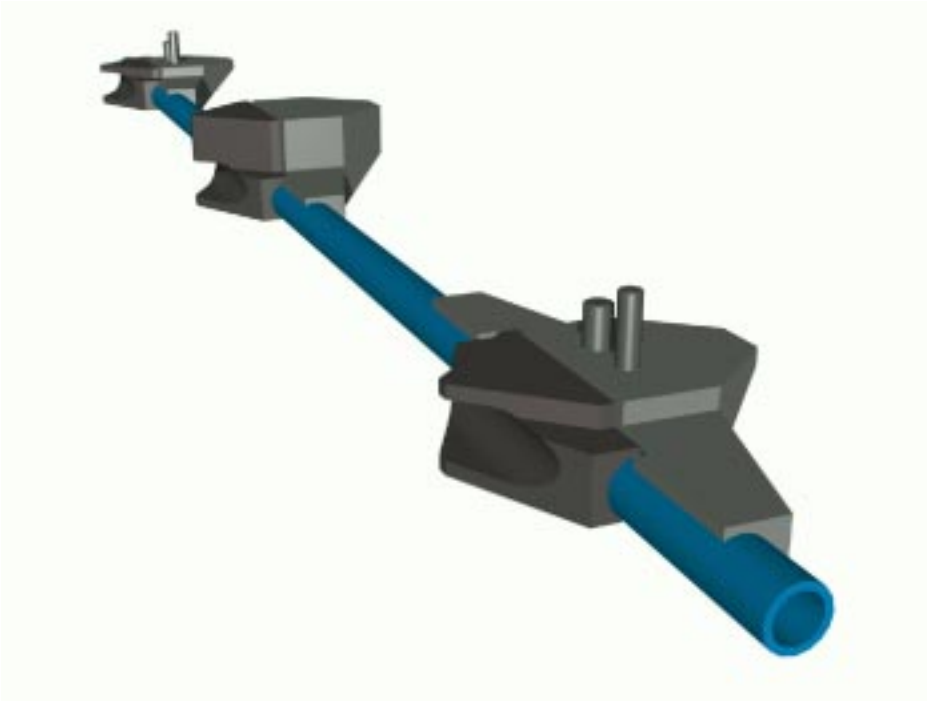

Figure 11: Full solid model of cooling pipe segment with two blocks for cooling lower modules and one for the module staggered on top. Pipe and blocks are glued onto the disk surface providing additional disk cooling against convection and radiation losses.

A cooling block also serves as a mechanical link between the disk and the module. This imposes many restrictions to the design which are not considered in full detail in our present work. The blocks have to enable precise fixation of the overlapping modules and therefore two different block heights are required (here: 6 and 10 mm resp.). The higher block should be less than 11 mm high to ensure the sensitive area of the disk to be hermetic. A second block at the end of the module, opposite to the hybrid, is used for precision fixing only, and obviously does not require cooling in our design.

The mechanical design of the cooling blocks of fig. 10 features a 1 mm gap length of the split. This is larger than the thermal fin length of 0.54 mm in the 50 µm thick CuNi pipe with the two-phase coolant (see Appendix A.1.6).

4.4 Connection between block and pipe

A glued contact between the block and the pipe must be avoided because the glue layer has a high thermal resistance in comparison with the resistance between pipe wall and fluid. NIKHEF engineers have demonstrated that a vacuum brazed joint could be made between a thin-wall stainless steel (316L+N recommended, also applied in cryogenics etc.) pipe and pyrolytic graphite, using an active alloy containing titanium. Figure 12 showing micrographs of the cross-section indicates that the active alloy completely fills the area between the pyrolytic graphite and pipe wall giving the joint excellent mechanical and thermal properties. The method was verified at CERN using a similar alloy.

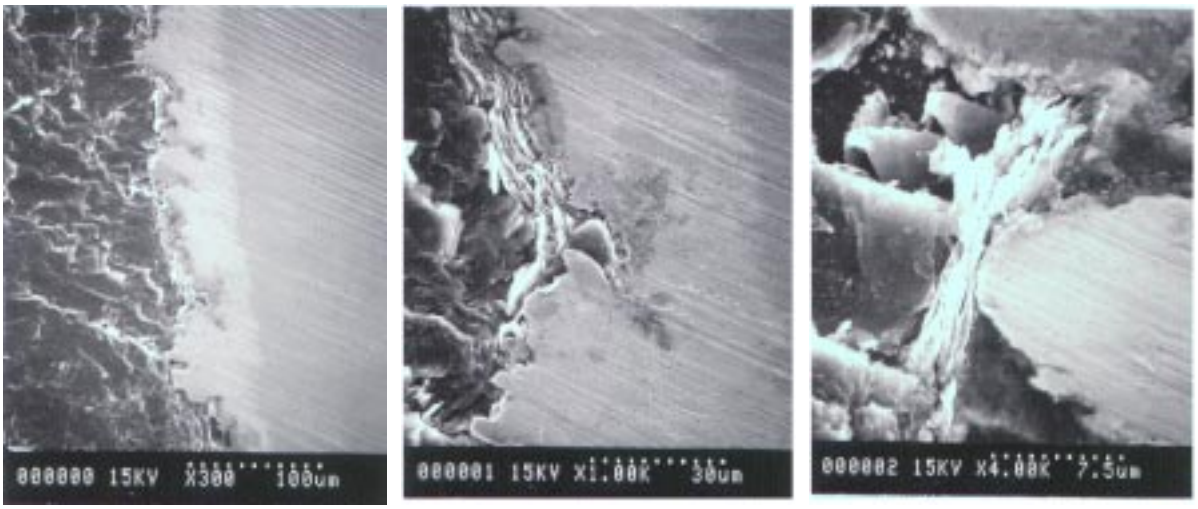

Figure 12: Micrographs of a stainless steel pipe vacuum-brazed to a pyrolytic graphite block without (copper) electroplating. The PG, solder area and pipe can be distinguished (from left to right) for three different magnifications (see text in pictures).

Carbon-carbon was also successfully vacuum brazed to a thin wall stainless steel pipe. In the photograph (fig. 13), the carbon fibres perpendicular to the pipe wall are clearly visible. The excellent mechanical connection between fibres and metal provides efficient heat transmission.

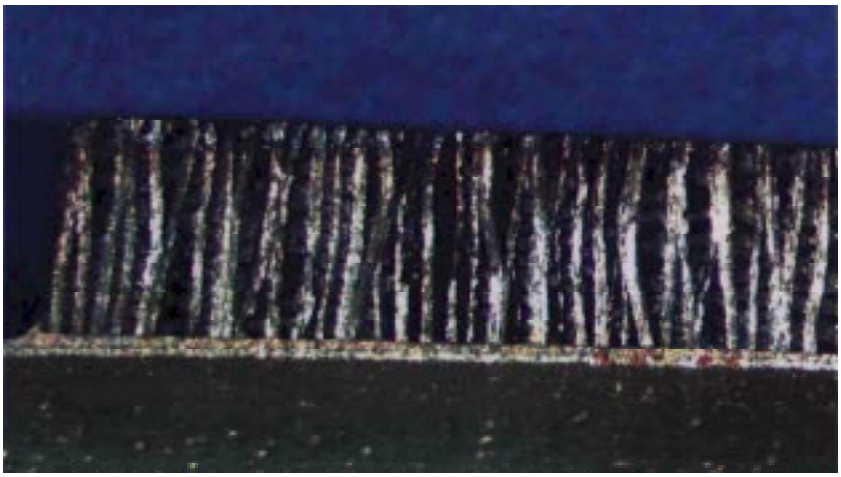

Figure 13: Photograph of a stainless steel pipe vacuum-braced to a carbon-carbon block (length ~ 1cm) without (copper) electroplating. The carbon fibres are perpendicular to the pipe wall.

The vacuum brazing technique was also tried at CERN with 70/30 CuNi pipe. However, the required brazing temperature is too high for this type of alloy. Therefore, the carbon-carbon composite was plated galvanically with Cu before soft-soldering the pipe onto the block[2]. Heating was accomplished with induction coil technique in air. The joints have excellent mechanical strength suggesting that the Cu plating adheres well to the C-C composite. Figure 14 shows micrographs of the cross-section of the circular CuNi pipe with 70 µm wall thickness, soldered to a split C-C composite block using SnAg solder. Clearly, the galvanic Cu coats the C-C very well, filling the microscopic cavities by capillary flow and adhering extremely well. The solder wets both the Cu and the CuNi materials, although minor cavities are visible in the photograph on the right. These may be due to the flux used or due to impurities. Additional tests are in progress with better solid-resin fluxes. Other solder alloys will be tried as well.

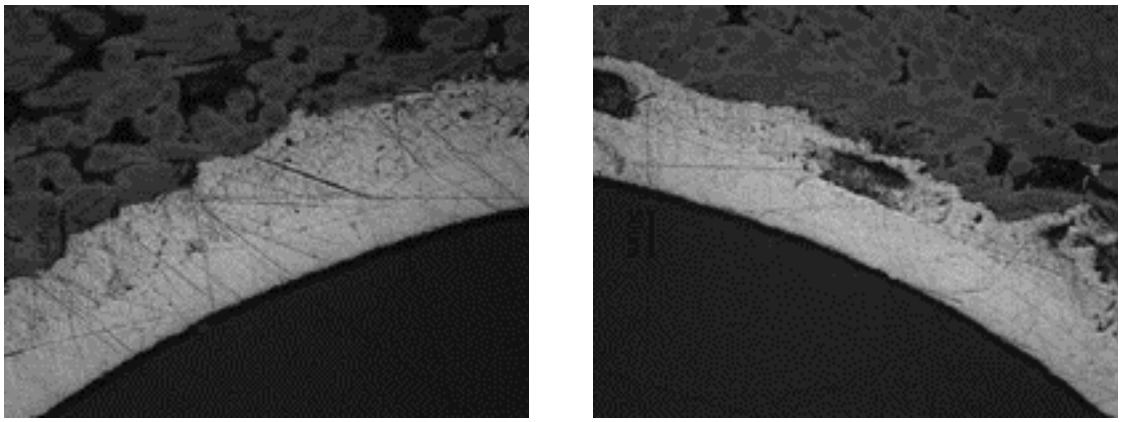

Figure 14: Micrographs of a CuNi pipe soldered to a split C-C block electroplated by a 15 µm layer of copper.

2 The work done by Serge Mathot/CERN-ST is gratefully acknowledged.

Tests are in progress to measure the thermal characteristics (resistance) of these joints and to examine them using metallographic methods.

The mechanical connection between the two block halves is partially given by their solder joints to the pipe, but mainly by their glued joints to the skin of the disk. Gluing the cooling structure requires dedicated jigging.

5. Thermal simulation of module and cooling block designs

The thermal behaviour of our modified module (fig. 8) was studied using an analogous electrical network model described in Appendix IV. This model includes linear (ohmic) resistors describing the thermal resistance between the nodes where the effective heat conduction behaves linearly. The heat transfer between the pipe wall and the coolant was simulated using a diode-type behaviour, numerically described by Eq. (5). The convection was simulated using a circulator, which conserves energy while allowing the convectional loss of heat from the hybrid to be different from the convectional heat load on the sensors. Coupling via the disk skin was omitted; its inclusion is possible but it only slightly improves the silicon temperature.

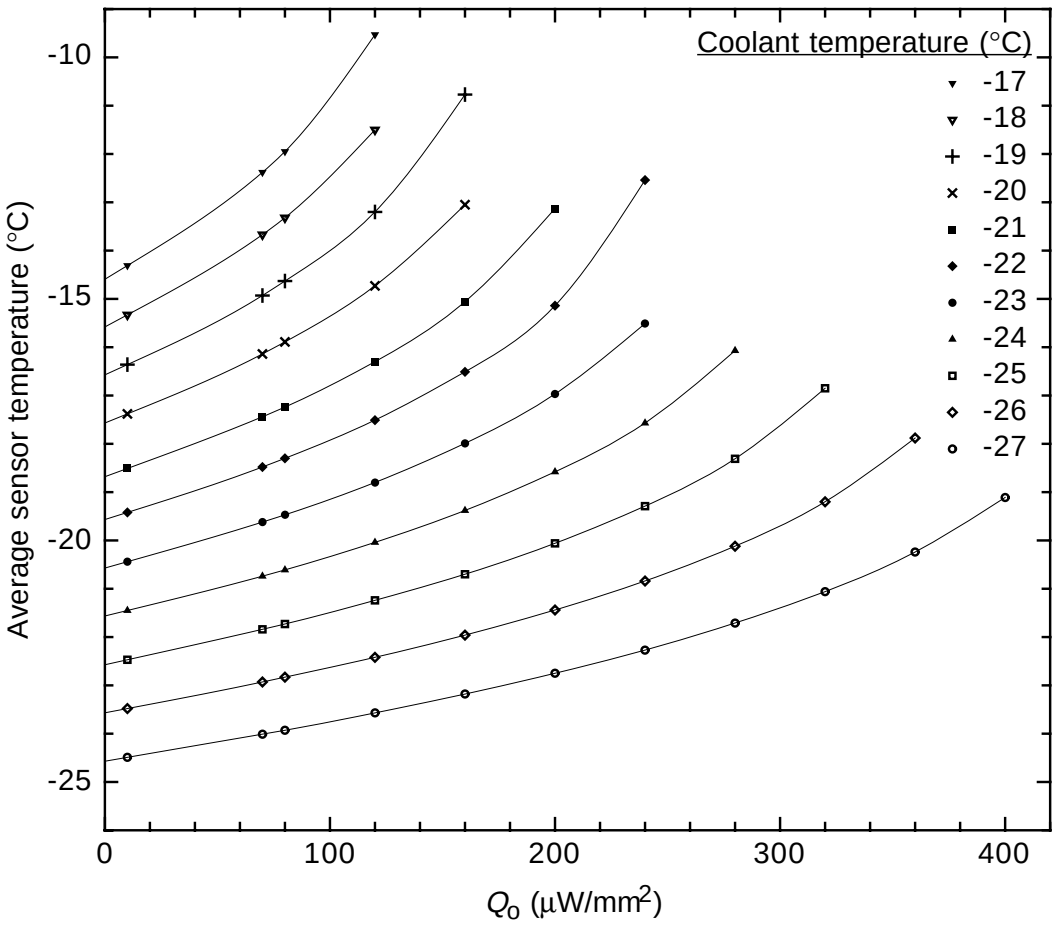

Figure 15: Evolution of the average sensor temperature (defined in the text) at constant coolant temperature, as a function of Q_o, the power density of the sensors at 0 °C.

The weak thermal couplings via the cooling pipe and ambient gas between the block sides were also included in the simulation. Their effect is almost negligible in comparison with the heat leak through the fan-ins. The thermal resistances in the model are listed in tables A4, A5 and A6 of Appendix IV. The thermal simulations show that with the full design power of eq. (1) (including the safety factor of 4 corresponding to the 0 °C power density of 240 μW/mm^2) the outer-ring modules are stable up to a coolant temperature of –21.7 °C. Operation in the first 5 years should therefore be possible at coolant temperatures around –17 °C. Afterwards, the temperature should be lowered progressively towards –23 °C if the most pessimistic scenario on the safety factors turns out to be realistic. This we believe however, seems very unlikely.

At minimum design temperature –27 °C of the coolant, the outer ring module can tolerate a power density of 400 μW/mm^2. Convection is included in the simulation.

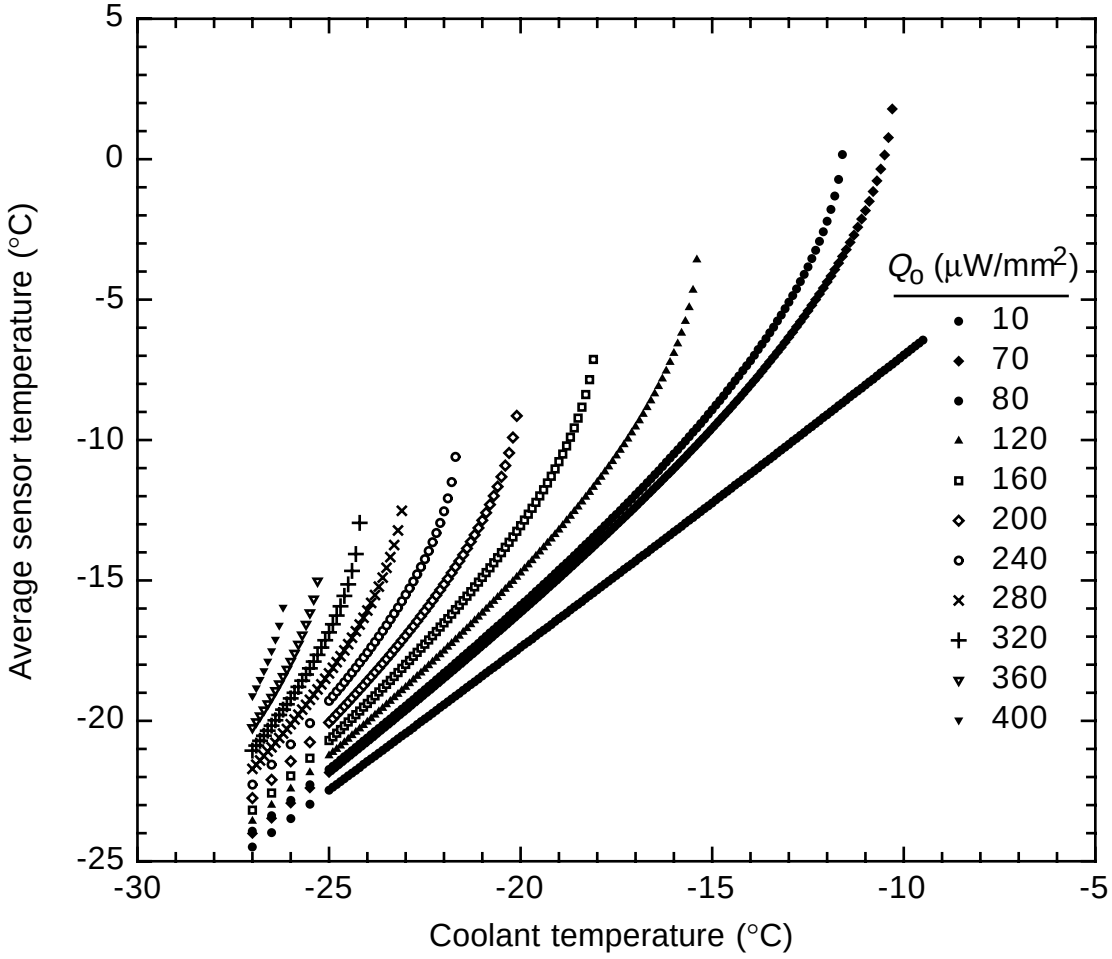

Figure 16: The average sensor temperature (defined in the text) as a function of the coolant temperature, at constant Q_o, the power density of the sensors at 0 °C.

Figure 15 shows how the sensor temperature evolves with increasing irradiation dose. The lines connect the points corresponding to the same saturation temperature of the coolant in the design range of –17 to –27 °C. The lines are cubic spline fits to the simulation data and serve only for guiding

the eye. The sensor temperature is defined as a constant temperature, which yields the same true power dissipation as the FEA calculation. This definition yields a power-weighted average temperature and is needed for the purpose of the thermal run-away simulation. As the temperature variation across the sensors is no more than 3.5 °C at the highest sensor power (~ 1.2 W), the deviation of the hottest-sensor point is less than 1.5 °C from our power-weighted average temperature. Under normal operating conditions the hottest point will be less than 1 °C above the average sensor temperature.

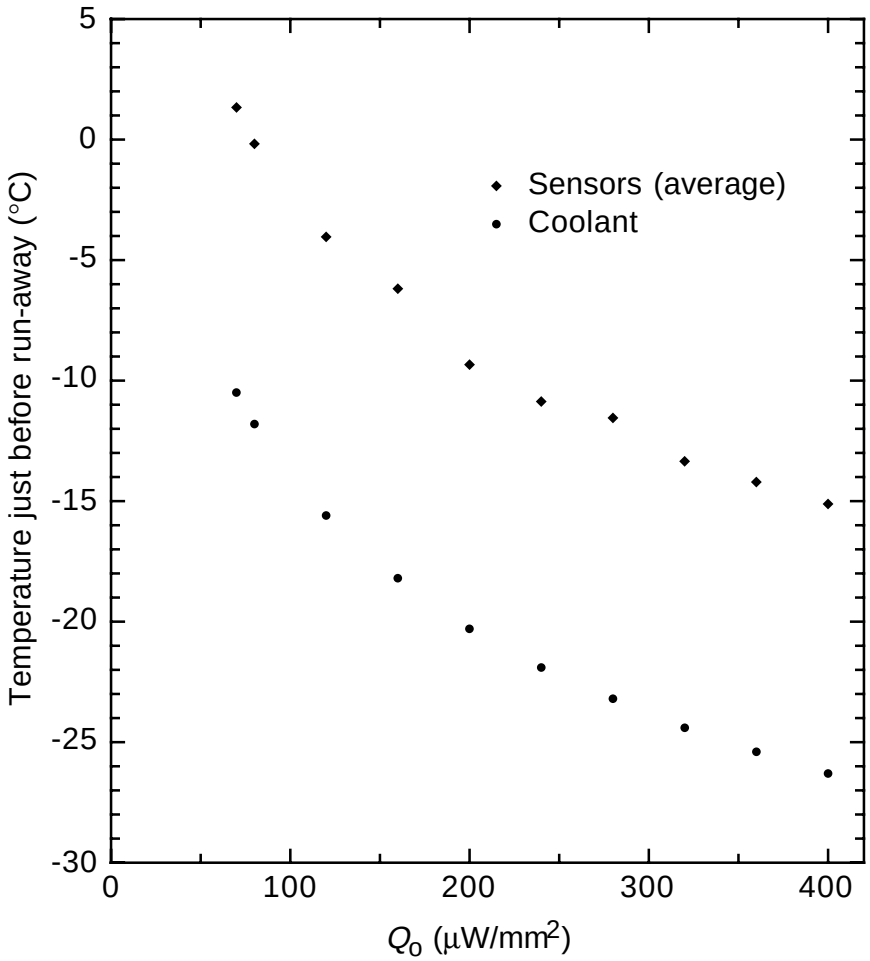

Figure 17: The temperature of the coolant and the average temperature of the sensors at the highest power density Q_o yielding stable operation in the simulation. The coolant temperature steps in the simulation were 0.1 °C corresponding to up to 1 °C changes in the sensor temperature near run-away. Therefore, the results on the sensor temperature appear to have more scatter than those on the coolant temperature.

A more practical view on the simulation results is shown by figure 16, where the average silicon temperature is plotted as a function of the coolant temperature, for different values of the sensor power density constant up to 400 μW/mm^2. It can be seen that no thermal run-away occurs at coolant temperatures below 10 °C, provided the power density constant is below 70 μW/mm^2. Similarly, at –17 °C a power density of 120 μW/mm^2 can be tolerated. The modules will therefore be stable at almost

twice the foreseen radiation damage resulting from 10 years of LHC operation, at the highest design temperature of the coolant. Under these conditions, the silicon temperature will not exceed –7 °C.

The thermal simulation reveals the most sensitive components in the heat transfer. In our current design these are firstly the contact region between the sensor block and the end of the unthinned TPG strip and secondly, the two-phase boiling resistance. The TPG strip was made slightly larger than the strip of the baseline design. This causes a temperature drop smaller than that of the boiling resistance, particularly at low and medium heat fluxes. The detailed breakdown of the thermal resistances is discussed in Appendix IV.

Figure 17 shows how the highest stable sensor and coolant temperatures evolve with the sensor power density. We stress that at coolant temperatures below –10 °C no run-away occurs for the 0 °C power densities of $Q_o < 70$ µW/mm^2.

The sensor power just below the run-away is 1.19 W at $Q_o = 240$ µW/mm^2 and depends quite weakly on the power density. At $Q_o = 70$ µW/mm^2, for example, it is 1.33 W and at $Q_o = 400$ µW/mm^2 it is 1.09 W. These values provide a near-ideal match with the maximum power output of the HV supplies. The detailed results on the various heat flows are discussed in Appendix IV.

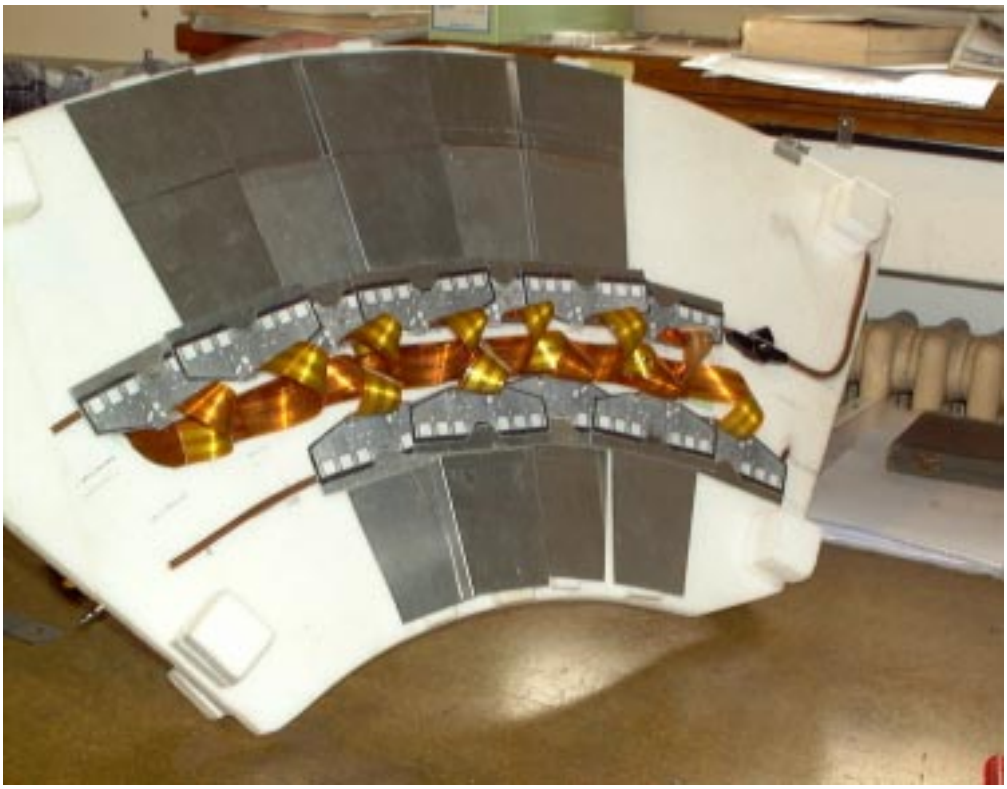

Figure 18: Disk sector mock-up including mechanical modules, cooling pipes and cables.

The thermal run-away model is very powerful for the mass optimisation of the modules while satisfying the thermal run-away specifications. The trustworthiness of these simulations is improved by parallel FEA simulation of the individual components of the heat paths. These yield a realistic effective thermal resistance of the objects with complex shape and thermal gradient field. Further work along

these lines, combined with explicit thermal measurements, may enable additional small mass reductions in the modules and cooling blocks.

6. Service layout

A partial disk (~ 60 ° sector) model was built (figure 18) in order to study and design an efficient and simple layout for the cooling system components, electrical cables and optical fibres. Our design has the fundamental difference with the baseline design that the power tapes cross over the cooling pipes that are glued to the skin of the disk.

The schematic layout of the cooling pipes was shown in fig. 1, together with the pipe connections and routing of the input and output lines at the bottom and top sectors of the disk. The simplicity of this layout is manifested in the number of holes which are required for running the pipes through the disk and in the accessibility of the disk surface for mounting, repair and changing the power tapes.

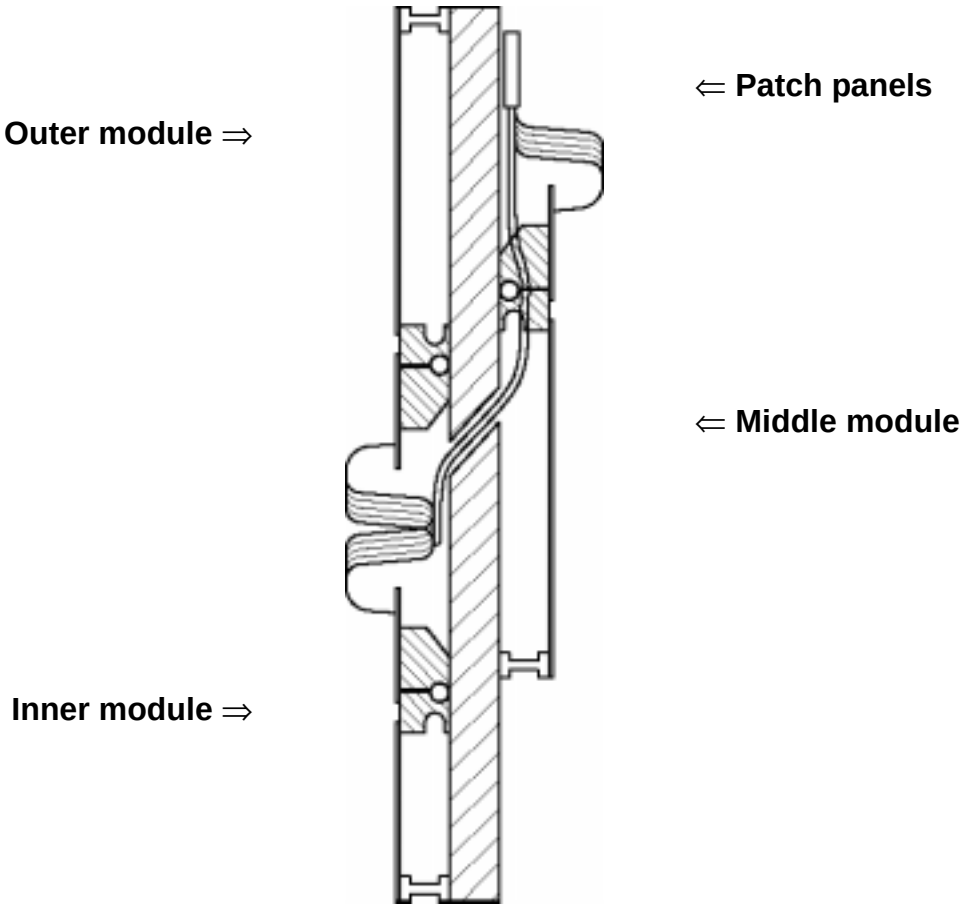

Figure 19: Power tape bundle routing through the disk.

The power tape routing over the cooling pipes and through the disk is shown in figure 19. The tape layout on the disk is illustrated in figure 20. It should be noted that in principle only two tape designs need to be manufactured, because the length adjustment is made by cutting the tapes. A complete set of engineering drawings showing the services can be found at the Web-address in ref. [6].

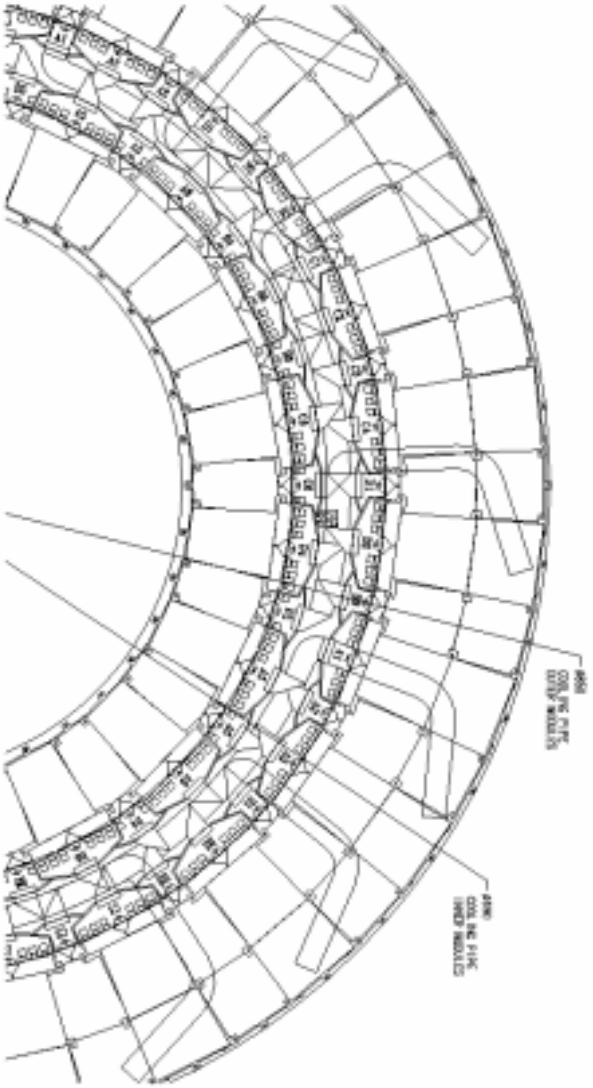

Figure 20: Power tape layout on the disk seen from the side of the inner and outer rings.

7. Material contribution to the thickness of the SCT detector

Our design of the cooling pipes and blocks is compared in table 4 with the ATLAS SCT ‘baseline’ design. A material thickness reduction factor of 4 is achieved. The baseline figures were presented at the Forward SCT Cooling Review by RAL in October 1999. Table 5 shows the radiation lengths used in the material evaluations. A 75% saving in the cooling pipe and block system is thus obtained.

Other designs following the baseline have been presented. However, simulations and measurements have not yet validated these somewhat less massive approaches for cooling pipes and blocks.

	Baseline			This work		
Item	Material	Volume (cm^3)	% of X_0	Material	Volume (cm^3)	% of X_0
Split block	Al	Sum =		C-C	222	0.131
End block	Al	441	0.641	PEEK	66	0.027
Pipes	Al	57	0.083	CuNi	5.16	0.046
Coolant[a]	C_3F_8	195	0.005	C_3F_8	90	0.002
Pads[b]	CFR	86	0.045	—	—	
Inserts[c]	PEEK	83	0.033	—	—	
Glue[d]	?	?	?	Epoxy	0.36	0.000
Pins, screws	SS, Al		0.020	SS, Al		0.000
Total			0.827			0.206

Table 4: Comparison of contributions to the multiple scattering for baseline and proposed cooling system. The calculations are based on distributing all materials over the active area of 7724 cm^2. — Notes: [a] The average amount of coolant has been evaluated at –22 °C coolant temperature using the method of Ref. [1]. Operation at temperatures differing by ±5 °C leads to ±15% change in the coolant contribution. [b] No cooling block pads are required in our design. [c] No mounting inserts are required in our design because the cooling blocks are glued directly onto the CFC skin. [d] In the baseline design no estimate was made for the glue required for the assembly of the cooling blocks.

Material	X_0 (g/cm^2)	X_0/ρ (cm)
Epoxy		25
Kapton		35
Carbon-carbon		22
TPG		19
CFC		25
Al		8.9
CuNi		1.44
AlN		8.4
PEEK		32
C_3F_8	34.6	

Table 5: Radiation lengths used in evaluating the effective contribution of the cooling pipes and blocks.

Table 6 shows the comparison of the contributions to the total disk thickness of the SCT TDR design, the present baseline design, and our proposed design. Comparing with the baseline, our design results in 30% reduction of the disk thickness.

In the baseline design the cooling pipes are made of aluminium and have an inner diameter of 3.6 mm and 0.2 mm wall thickness. The cooling pipe system involves many more parallel pipes and connections. The mass of the pipe unions was not evaluated, because there is no tested method yet for the joining of such thin-wall aluminium pipes. It has been proposed to make glued joints, but their reliability is highly questionable because the fluorocarbons cause swelling and shrinking of the proposed epoxies. Moreover, leak testing of epoxied joints is impossible using helium mass spectrometry.

Item	TDR	Baseline	This work
Disk	0.527	0.248	0.248
Cooling/fixing blocks	0.119	0.641	0.158
Mounting inserts	0.012	0.033	—
Fasteners/pads/glue	0.008	0.065	0.000
Cooling pipes	0.137	0.083	0.046
Coolant	0.095	0.005	0.002
Modules	1.529	1.459	1.336
Cabling	0.170	0.170	0.100
Total	2.597	2.704	1.890

Table 6: Contributions to the total disk thickness measured in the terms of the percentage of the radiation length. The patch panels, the disk supports and the demountable pipe unions are not included in any of the estimates; these are located at or close to the outer radius of the disks.

8. Engineering status, plan of work and impact on SCT schedule

8.1 Engineering and prototyping

The disk layout as depicted in figure 1 has been engineered in detail using 3D modelling software [5]. A two-dimensional projection of the inner and outer module arrangement on the disk was presented in fig. 18. Below, in figure 21, the design of a section of the opposite side of the disk is given. In figure 22 a photograph of the mock-up is shown. Also here the cables are routed circumferentially before they expand radially from the middle ring modules to reach the patch panels. Sufficient area remains to mount patch panels either parallel or perpendicular to the disk surface. The orientation and the necessity of having patch panels are subject to the design of the disk support structure and disk assembly procedure.

Obviously, an installation procedure that could avoid having patch panels for power tapes and

cooling pipe connectors at the outer rim of the disks would further reduce the material in front of TRT and calorimeters.

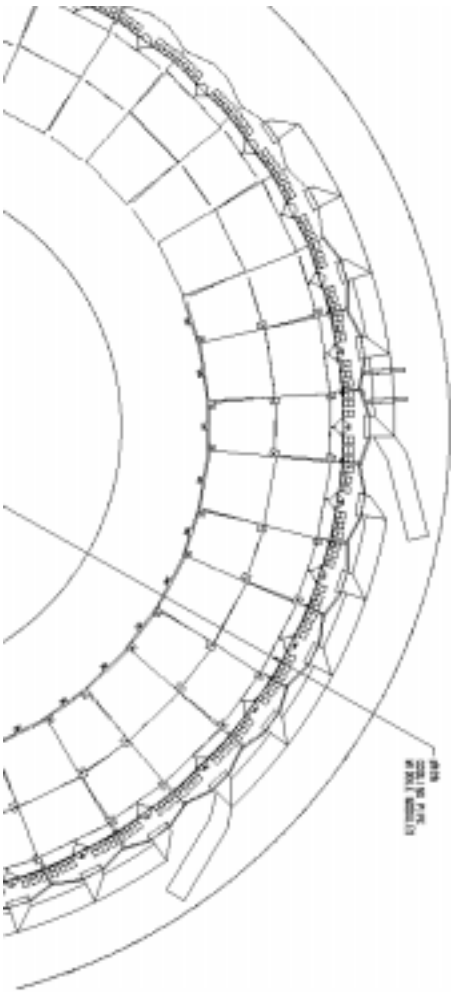

Figure 21: Power tape layout on the disk seen from the side of the middle ring.

A section of a carbon-fibre honeycomb disk has been produced to facilitate a system test. Several forward SCT modules will be operated (full optical readout) together (see fig. 23a). The disk is equipped with both baseline aluminium wiggly cooling channels and a circumferential thin wall stainless steel carbon fibre reinforced cooling cannel (fig. 23b). The pyrolytic graphite cooling blocks are vacuum brazed to the stainless steel.

By adjusting the fibre and/or resin composition of the pipe wrapping, the CTE of the hybrid channel can be tuned. With ESPI, the carbon fibre honeycomb structure has been analysed and measured by the Oxford group [7]. The average CTE of the panel was found to be ~ 2 ppm/K.

Figure 24 shows the linear behaviour of a hybrid channel under temperature variation with CTE of 1.5 ppm/K. Measurements have been calibrated using a bare stainless steel channel and a solid carbon fibre pipe (CTE = –4 ppm/K !). Several samples have been produced of which some have been extensively temperature cycled (> 100 times) between –40 ^{0}C and +25 ^{0}C. No signs of fatigue have

been observed.

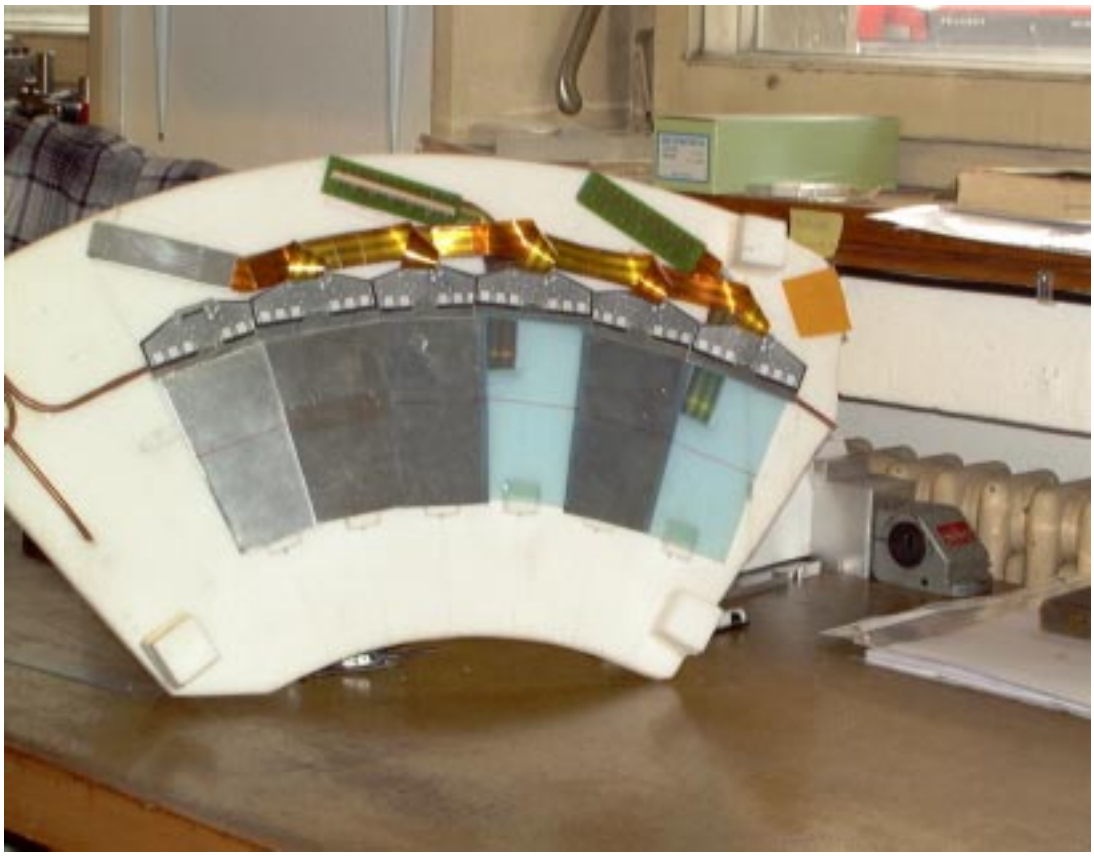

Figure 22: Photograph of disk sector mock-up showing the middle ring modules, cooling, cables and patch panels.

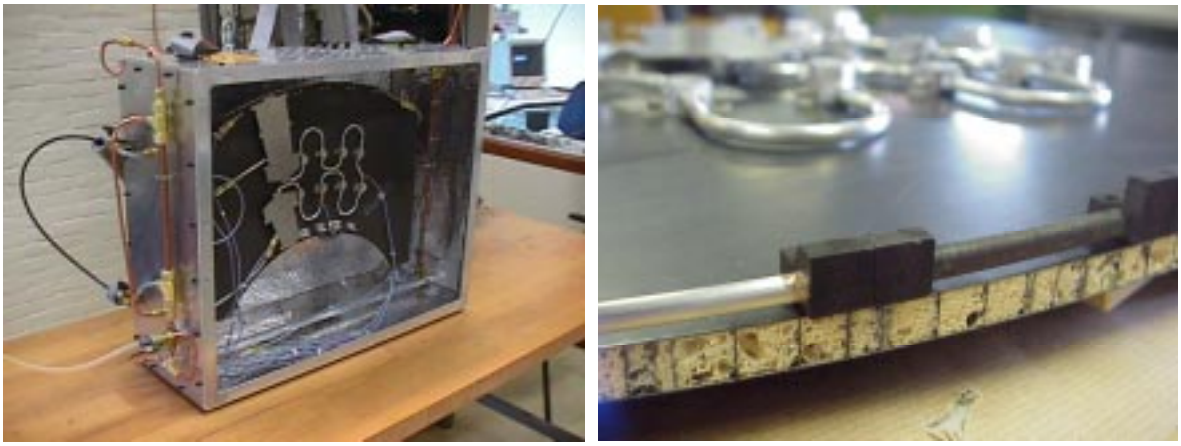

(a) (b)

Figure 23: Carbon fibre honeycomb disk segment for testing forward silicon strip modules (a). The sector is equipped with wiggly aluminium cooling channels with aluminium cooling blocks. The outer sensors are cooled by a carbon fibre stainless steel hybrid channel) and cooling blocks made of pyrolytic graphite (b).

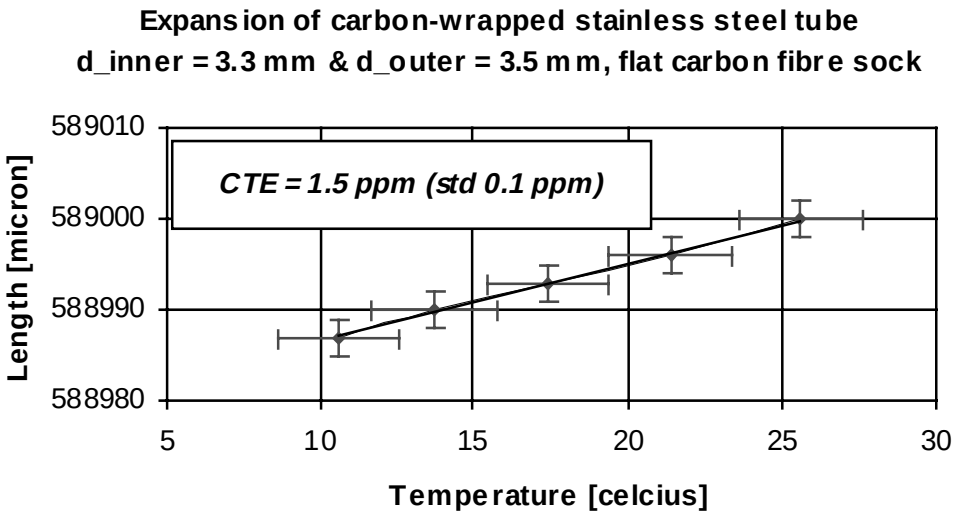

Figure 24: Thermal expansion measurement on carbon fibre reinforced stainless steel tube. The tube has an outer diameter of 3.5 mm and a wall thickness of 100 μm. By a proper choice of fibre and resin, the CTE can be tuned to match the CTE of the support disk.

Anticipating our split cooling block design and the various advantages of CuNi, several cooling blocks were fabricated. As the block design evolved over time, all blocks slightly differed from the design presented in figures 6 and 9. Of these, seven were made of Cu and three of C-C composite. For the three C-C blocks, different orientations for the worst heat conducting direction were chosen. A series of new C-C blocks for mounting on 3.7 mm diameter CuNi pipe is in production now. Engineering drawings of the blocks can be found on the Web as well [6].

The far-end of the module (the sensor side) will be supported by blocks made of PEEK. Aluminium prototype supports exist.

Two dummy modules were built and their mechanical stability was demonstrated. One of the modules was measured at +22 °C, +36 °C and –13 °C. Mechanical distortions were found very small. 3D-drawings of the modified module design exist.

8.2 Plan of work

In the joint effort of SCT for the End-cap cooling, it was decided to draft a plan for studying the various alternatives of disc layout and thermal design. A stock of CuNi pipes, with 3.7 mm outer diameter to be used in these tests, was ordered and will be delivered around the 5th of June. The pipes will be used for bending and burst tests, and for optimising the solder joint techniques with the C-C blocks and with the pipe unions. Some of the pipe bending and solder joining tests will be performed in collaboration with the CMS experiment which is also proposing to use CuNi pipework in their tracker cooling.

The prototype C-C cooling blocks for the circumferential pipe layout will be machined at the University of Geneva. The soldering development and production will continue at CERN. Industrial-scale machining was also investigated and offers were received indicating that the machining cost for the full amount of cooling blocks will result in less than 35 DM/block.

The thermal tests of a prototype pipe sector are planned during July-August 2000. In these tests the heat transfer coefficient will also be measured more precisely as a function of heat flux and quality factor. Thermal modules will be mounted on the prototype C-C blocks and the entire heat conduction path will be characterised and compared with the FEA results. The thermal run-away conditions will be verified in these tests in order to check the model used in our present simulations.

Thermal outer-ring modules will be assembled in the University of Geneva for the above tests. Here the real module materials and assembly techniques will be used.

8.3 Impact on the SCT schedule

The proposed small modifications to the silicon module will hardly affect its assembly time. Modifications to the assembly jigging remain minor while the SCT has already agreed to implement some of the changes.

The simplicity of our pipe routing, resulting in a much more simplified service layout, justifies investments in this alternative route. The reduced number of machining steps and finally, fewer assembly components, will shorten the wheel production cycle substantially. Moreover, considerable progress has already been made in parallel to baseline developments.

Whether the work plan proposed above will interfere with further baseline activities remains to be seen. Many components are already available now (full-scale prototype support disk) or will become available soon (thin wall CuNi piping and C-C cooling blocks). Several development steps can be regarded as complementary to baseline developments.

9. Summary and conclusions

In this paper, we have reported on investigations for optimising the cooling, service layout and the local mechanical support of the forward SCT modules. The study was motivated by the serious criticism of the LHCC on the material budget of the baseline design. Less material and therefore a longer radiation length demands an approach in which mechanical stability and precision, thermal performance and service layout for both the modules and disk support structure are considered at equal footing. We have limited ourselves to the analysis of the forward disks. A more global approach, including support cylinder, thermal enclosure –is an active thermal enclosure required ?- is still urgently needed.

The first step in the optimisation procedure was the reduction of the number of cooling pipes per module. We have demonstrated that this can be achieved by introducing minor modifications to the

present module design and optimisation of the module-cooling pipe connection. The baseline C_3F_8 evaporative cooling system and cooling pipe diameter obviously allow for single pipe operation in terms of heat flux.

The second step involves the observation that the module support structure (disk) should be very stiff and should have a small (close to 0) CTE for thermal and mechanical stability. This can be achieved by using a homogenous 10 mm thick carbon fibre honeycomb structure in which extremely thin ($3 * 60$ μm) skins are applied. Transmission of forces, except for the forces due to the natural weight of both modules and services, should be avoided since the low mass disk achieves a good stiffness in the fibre directions only. The present baseline intends to reduce the forces (and moments) due to expansion and contraction of the cooling pipes by introducing 'wiggles'. However, some forces remain (of order 12 N per cooling point fixation). Obviously, introducing additional pipe length is at the expense of increasing the mass. To transmit the remaining forces to the disk without losing module position precision can in the baseline only be achieved by introducing a substantial number of inserts.

The inserts introduce mass and destroy the properties of the thin skin: at each hole the fibre structure is cut and has to be reinforced by a glue connection between fibres and insert. By absorbing the contraction and expansion forces in the cooling channel itself, this can be avoided. A hybrid-cooling channel therefore not only avoids 'wiggles' but also simplifies the disk manufacturing. The disk integrity is kept: cooling channels can be glued directly to the disk and precision inserts can be added to the cooling blocks after they have been mounted. Reduced channel lengths will now also allow for reducing the number of channels per disk with some obvious advantages: more room to optimise service layouts on both disk and support cylinder.

In conclusion, our alternative disk design achieves:

- Considerable material savings in:
  - cooling system (> 75%)
  - total forward structure (~ 30%)
  - more homogeneous spread of massive parts (mass concentration will cause inefficient spots on the disk)
- Improved reliability:
  - thermal run-away avoided by safety factor of 4 at coolant temperature below –21.7 °C (the safety can be improved by simply lowering the coolant temperature)
  - non-corroding pipes, safe solder connections, no small-radius bending of pipes, low manifolding multiplicity
- Better uniformity of the temperature of the sensors compared with the baseline two-point cooling:
  - mainly due to one single cooling pipe connection
  - also due to the better thermal conduction in the TPG strip
  - in the baseline the sensors are mainly cooled at the far end and heated by the hybrid at the opposite end; this leads to a large thermal gradient in the sensors

- Reduced complexity in construction:
  - less R&D required
  - reduced manufacturing time
  - blocks glued to disk deliver precise location of module
  - reduced number of parallel cooling channels and manifolding
  - uniform pipework design for all disks
  - manpower and cost savings
  - simplified test structure for system tests
- Better disk integrity:
  - only few 'service' holes required
  - only two 'basic' power tape designs required (power tapes only differ in length)
  - mechanical stresses by power tapes to the module are avoided
- Full hermeticity:
  - distance between 'front' and 'back' module within specifications

The following issues need further attention:

- Forces due to thermal expansion of the cooling circuit may require an encapsulation of the cooling pipe with carbon fibre. To our knowledge, there is no experience in stressed glue connection between metal and carbon fibre in high-radiation environment.
- Although we are confident that our design is viable, the thermal performance of this alternative layout has not been tested. The layout and the implications on the module have been modelled and we are fully confident that the thermal design is well within requirements. It has to be mentioned that the thermal performance of the base-line design is not yet proven in a full-scale set-up either.

All these arguments lead us to propose to equip an (already existing) full-scale prototype disk with a large radius circumferential cooling channel including soft-soldered carbon-carbon blocks. We envisage that, due to the simplicity of the structure, thermal and mechanical properties can be reported still during summer 2000. Except for the need of an evaporative cooling facility, we expect no interference with the present schedule. It can even prove to be very beneficial to the production schedule already this summer, since our design contains fewer components and less machining of mechanical supports.

10. Acknowledgements

We would like to thank Mr. Serge Mathot of CERN for his important contributions in the development of the soldering techniques of CuNi pipes onto C-C blocks. The help and support of Prof. Allan Clark, Mr. Eric Perrin and their team of the University of Geneva are gratefully acknowledged. The NIKHEF technical staff, in particular: Mr. Henk Schuijlenburg, Mr. Jarl Buskop, Mr. Niels Sijpheer, Mr. Hans Band and Mr. Jan Homma have given important comments and advice in engineering and construction issues. One of us (H.B.) would also like to thank Mr. Hans Dietl for numerous discussions and critical comments. The help of the ATLAS cooling team was valuable for the thermal measurements. Finally, we thank Richard Fortin for providing drawings of modules and his advice on their assembly.

Appendix I: Two-phase calculations

A.I.1 Expansion orifices

The expansion of a sub-cooled liquid through a sharp-edge orifice happens at the discharge rate of

$$\dot{m} = \rho \dot{V}_\ell = \frac{\pi D_2^2}{4\sqrt{1-(D_2/D_1)^4}} C_d \sqrt{2 g_c \rho_\ell (p_1 - p_2)} \qquad \text{(A1)}$$

where D_1 and D_2 are the diameters of the pipe upstream of the orifice and the orifice itself and the discharge coefficient C_d = 0.58 for the ratio D_2/D_1 = 0.25 when the Reynolds number in the orifice is above 10^4. The pressures upstream and downstream of the orifice are p_1 and p_2, respectively, and g_c = 1 = 10^6 $gs^{-2}cm^{-1}$/bar. The orifice diameters in table 2 are calculated for $p_1 - p_2$ = 5.0 bar and liquid density 1.533 g/cm^3. The ratio of the orifices should be 1.134 to yield a mass flow ratio of 2.7/2.1.

When the same tool is used for machining the orifices, it is easy to match the discharge rates of the orifices to better than 5%. If this is not sufficient, the relative discharge rates can be measured by feeding parallel orifices from a common pressure supply. By measuring the resulting mass flow rates using a thermal mass flow meter with low pressure drop, such measurements can be made to a relative accuracy better than 1%. The rates of orifices of different sizes can be measured to the same relative accuracy.

Eq. (1) shows that the mass flow rates can be controlled by the feed pressure and that the ratios of the mass flow rates will remain unchanged. The accuracy of the theoretical mass flow rates is somewhat deteriorated if the downstream pressure is such that the fluid enters the two-phase region. This is, however, a small effect in a sharp-edge orifice because vapour bubbles are only formed at a distance of several pipe diameters from the orifice.

If expansion capillaries are used, the situation is quite different. Depending on the length of the capillary, vapour will be formed and the pressure drop will be controlled both by flow friction and by fluid dynamic effects caused by expansion. The mass flow rate will depend more on the temperature than on the pressure upstream when the pressure exceeds a certain limit. Under these conditions, the ratio of the flow rates through two different capillaries is not constant when the flow rates are varied by controlling the upstream pressure. The capillary expansion devices must therefore be tested using the actual coolant fluid for the entire range of operating parameters. The flow through the capillary could thus be controlled also by the extent of subcooling upstream, but this requires a rather elaborate control and monitoring system.

A.I.2 Pressure drop

The pressure drop in two-phase flow inside a heated tube arises from flow friction and from fluid dynamic effects, which are due to the increased momentum of the heated fluid. In homogeneous two-phase flow, the frictional pressure gradient can be calculated. For instance, one can use the Lockhart-

Martinelli correlation as in Ref. [1] or the Chisholm equation. The latter, see Eq. (A2), is simpler and gives more physical insight. Both approaches are, however, equivalent in the terms of numeric results and accuracy.

The two-phase momentum pressure drop arises from the acceleration of the fluid when the vapour fraction increases in the heated sections of the cooling pipe. The sum of the two pressure gradients can be integrated to yield the dynamic pressure at the locations of the cooling blocks. This dynamic pressure can be used to calculate the fluid temperature from the saturated vapour pressure equation.

In integrating the pressure gradient over the entire length of the cooling pipe, one should take into account the cooling of the fluid, which is the consequence of the drop of the dynamic pressure. The fluid properties should be calculated at the temperature corresponding to this dynamic pressure, so that the pressure gradient would be correct. In the range of our pressure gradients, however, this second order effect is very small. The resulting small overestimate in the total pressure drop is compensated by our integration procedure, which consists of taking the pressure gradient to be constant between cooling blocks. The value is calculated at the first one. A more accurate Runge-Kutta procedure would result in a larger total integration error because it would lack the compensation due to the changes in the fluid parameters.

The pressure drop can only be calculated under the assumption that the flow is homogeneous; i.e. those vapour and liquid phases are well mixed. At low fluid speed, the flow pattern may become intermittent and therefore the pipe diameter must not be made too large. Moreover, it is desirable to maintain a reasonable pressure gradient in the pipe. This will lead to an output temperature sufficiently lower than the input temperature, which can be used for compensating the convectional heat load variations between the various module locations on the disks. With the Baker map, it was verified that the flow is indeed in the homogeneous annular mist regime under all operating conditions except at the lowest *x,* for which the flow is in the homogeneous bubbly regime. The Taitel and Dukler correlations confirm that only at low *x* the flow is marginally in the bubbly regime.

A.I.3 Chisholm equation for frictional pressure drop in two-phase flow

In the following, we shall estimate the frictional pressure drop in homogeneous two-phase flow using the Chisholm equation [4]

$$\left(-\frac{dp}{dz}\right)_{TP} = \left(-\frac{dp}{dz}\right)_{\ell} + C\left[\left(-\frac{dp}{dz}\right)_{\ell}\left(-\frac{dp}{dz}\right)_{g}\right]^{1/2} + \left(-\frac{dp}{dz}\right)_{g} \qquad \text{(A2)}$$

which relates the two-phase pressure gradient (index *TP*) to that with the liquid and gas fractions flowing alone at the mass flow rates $(1 - x)\dot{m}$ and $x\dot{m}$, respectively. Here the Chisholm parameter *C* depends on the Reynolds numbers of the liquid and gas flow rates and is obtained from the table below.

Liquid flow	Gas flow	*C*
turbulent	turbulent	20
laminar	turbulent	12
turbulent	laminar	10
laminar	laminar	5

Table A1: Chisholm parameter C for different flow regimes.

For the pipe designs presented in this paper, the gas flow downstream the expansion orifice is always turbulent because the quality factor is around $x = 0.05$ in this region. The liquid flow is always laminar, apart from the region of the first few modules where the liquid flow is in the transition region between laminar and turbulent. Therefore, we have chosen to use $C = 12$ in our numeric calculations. This choice results in a numeric underestimate of the pressure gradient up to 20% at the beginning of the pipe. This is compensated by the way we estimate the friction factor, as will be discussed below.

The single-phase pressure gradients can be obtained from

$$\left(-\frac{dp}{dz}\right)_\ell = f_\ell \frac{(1-x)^2 G^2}{2D\rho_\ell}$$
$$\left(-\frac{dp}{dz}\right)_g = f_g \frac{x^2 G^2}{2D\rho_g} \qquad \text{(A3)}$$

where G is the total mass flow per cross-sectional area and D is the hydrodynamic diameter of the tube (the diameter itself for a circular tube). f is the friction factor calculated here for the liquid and gas fractions from

$$f = \frac{64}{N_{\mathrm{Re}}} + 0.184 N_{\mathrm{Re}}^{-0.2} \qquad \text{(A4)}$$

which is the sum of the friction factors for laminar and turbulent flows. This overestimates the liquid and gas pressure drops in the transition region around $N_{\mathrm{Re}} = 2300$ and results in an overestimate of the two-phase pressure gradient up to about 30%. This overestimation is quite accurately compensated in the pressure gradient by using $C = 12$ throughout the tube. The errors due to these two approximations almost cancel and yield an overestimate of less than 5% in the total pressure drop. This remaining overestimate on the other hand, will be compensated by the integration procedure described below.

The Reynolds numbers for the liquid and gas flows, for the liquid and gas flow friction factors, are

$$N_{\mathrm{Re},\ell} = \frac{(1-x)GD}{\eta_\ell} \qquad \text{(A5)}$$

and

$$N_{\mathrm{Re},g} = \frac{xGD}{\eta_g} \tag{A6}$$

where η is the viscosity.

A.I.4 Momentum pressure drop

The gas dynamic pressure gradient is mainly due to the increase of the fluid momentum with the quality factor following heat input and evaporation. This can be expressed analytically and integrated over the heated area. By denoting the gas fraction just before and just after a short heated area with x_1 and x_2, the momentum pressure drop can be written [5]

$$\Delta p_m = \Phi_m \frac{\dot{m}^2}{A^2 \rho_L} 10^{-6} \frac{\mathrm{cm\,s}}{\mathrm{g}} \mathrm{bar} \tag{A7}$$

where

$$\Phi_m = \frac{(1-x_2)^2}{R_{\ell 2}} - \frac{(1-x_1)^2}{R_{\ell 1}} + \left[\frac{x_2^2}{R_{g2}} - \frac{x_1^2}{R_{g1}} \right] \frac{\rho_\ell}{\rho_g} \tag{A8}$$

only depends on the difference between the input and output quality factors. In the above formula $R_{\ell g}$ are the volume fractions of the liquid and gas at points 1 and 2, respectively.

A.I.5 Chen's dimensionless correlations for heat transfer in two-phase flow

We shall now discuss the heat transfer coefficient which is defined as $h = \dot{Q}/(A_h \Delta T)$ and which relates the heat flux to the difference between the heated wall temperature and the average temperature of the flowing fluid. The heat transfer to the flow of a boiling liquid is much higher than to the flow of sub-cooled fluid, owing to the fact that two efficient mechanisms work in parallel. The two-phase flow heat transfer coefficient [4]

$$h_B = h_{NB} + h_{FC} \tag{A9}$$

is the sum of terms due to nucleate boiling on the pipe wall and to forced-convection heat transfer through the thin liquid film covering the tube wall in the annular flow regime. The nucleate boiling term can be obtained from the Forster-Zuber equation for pool boiling and the two-phase flow suppression factor *S*

$$h_{NB} = Sh_{FZ} = S \cdot 0.00122 \Delta T_{sat}^{0.24} \Delta p_{sat}^{0.75} \frac{C_{pL}^{0.45} \rho_L^{0.49} \kappa_L^{0.79}}{\sigma^{0.5} L_0^{0.24} \eta_L^{0.29} \rho_G^{0.24}} \tag{A10}$$

where ΔT_{sat} is the difference between the saturation temperature of the flowing fluid and the

temperature of the tube wall and Δp_{sat} is the difference between the pressure of the flowing fluid and its saturation pressure at the wall temperature. The suppression factor *S* is a function of the liquid Reynolds number and is a universal parameter for all fluids. It is clear that the nucleate boiling term of Eq. (A10) is not a constant but depends on the temperature difference. Further complications arise from the fact that the wall characteristics influence the magnitude of the nucleate boiling term. These lead to an uncertainty of about ±40% in the heat transfer to the flow of a boiling fluid.

The forced convection part can be determined from

$$h_{FC} = Fh_L \tag{A11}$$

where *F* is the two-phase flow heat transfer coefficient multiplier and h_L is the single-phase flow heat transfer coefficient, which is proportional to the Nusselt number

$$Nu_L \equiv \frac{h_L D}{\kappa_L} = 0.023 N_{\mathrm{Re},L}^{0.8} N_{\mathrm{Pr},L}^{0.4} \tag{A12}$$

where the liquid Reynolds number is

$$N_{\mathrm{Re},\ell} = \frac{(1-x)GD}{\eta_\ell} \tag{A13}$$

In addition, the liquid Prandl number is

$$N_{\mathrm{Pr},\ell} = \frac{\eta_\ell C_{p\ell}}{\kappa_\ell} \tag{A14}$$

The multiplying factor *F* in Eq. (A1) is a universal dimensionless function of the Martinelli parameter *X*. The functions *F* and *S* are also given in Ref. [1] together with the fits used in evaluating the two-phase flow heat transfer coefficient. At a fixed mass flow rate, both functions only depend on the quality factor *x*.

The dimensionless correlations of Chen were used to determine the heat transfer coefficient at mass flow rate of 2.7 g/s in a pipe of 3.5 mm inner diameter. This flow rate corresponds to the outer ring cooling pipe; the inner and middle ring pipes have a flow rate of 2.1 g/s which yields a few percent smaller heat transfer coefficient. We consider this effect small in comparison with those due to the quality factor, shown in figure 3 for three coolant input temperatures and heat flux of 4.5 W/cm^2.

When evaluating the thermal stability of the modules, the relationship between the heat flux and the temperature drop is required. We can evaluate this by summarising the above in the form

$$\begin{aligned} h_B = {} & 0.023(1-x)^{0.8}\left(\frac{GD}{\eta_\ell}\right)^{0.8} \mathrm{Pr}_\ell^{0.4}\, F(x) \\ & + BS(x)(\Delta T)^{0.24}\, p_{sat}^{0.75}\left[\exp\left(\frac{L^o}{R}\left[\frac{1}{T_{sat}} - \frac{1}{T_{sat}+\Delta T}\right]\right) - 1\right]^{0.75} \end{aligned} \tag{A15}$$

where the dependence on x and ΔT has been shown explicitly by using the vapour pressure equation. The constant B is the remainder of the Forster-Zuber equation after factoring out $S(x)$ and the powers of the saturation pressure difference and saturation temperature difference. We notice that the first term depends only on x, whereas the second depends on both x and ΔT.

The factor containing the exponential can be approximated by a Taylor series expansion and keeping only the first term in the series after subtraction of 1. Denoting the constant factors by B_2 and B_1, the dependence on x and ΔT becomes

$$h_B = B_2 (1-x)^{0.8} F(x) + B_1 S(x) (\Delta T)^{0.99} \tag{A16}$$

Replacing the power 0.99 by 1.00 and recalling the definition of h, the heat flux can be approximated by

$$\frac{\dot{Q}}{A} = h_B \Delta T = \Delta T \left[B_2 G(x) + B_1 S(x) \Delta T \right] \tag{A17}$$

where $G(x) = (1-x)^{0.8} F(x)$. This is a simple second order equation, which can be inverted

$$\Delta T = \frac{B_2}{2B_1} \frac{G(x)}{S(x)} \left[\sqrt{\frac{4B_1 S(x)}{B_2^2 G^2(x)} \frac{\dot{Q}}{A} + 1} - 1 \right] \tag{A18}$$

Here the constants and functions are from fits to the two-phase dimensionless correlations and are given at a temperature of –22 °C by

$$\begin{aligned} B_1 &= 4.28 \cdot 10^{-2} \\ B_2 &= 4.03 \cdot 10^{-2} \\ G(x) &= \left[1.87 x^{0.65} + (1-x)^{0.63} \right]^3 \\ S(x) &= \left(1 - 1.67 \cdot 10^{-2} x + 0.21 x^4 \right) (1-x)^{0.1} \end{aligned} \tag{A19}$$

Figure A1 shows the temperature difference between the pipe wall and the coolant for the outer ring pipe at –27 °C coolant temperature, as a function of the heat flux. We note that for high power dissipation in the sensors, the temperature difference is about 2°C higher than for low power dissipation. Higher power dissipation corresponds to modules at the top of the disk. These receive a larger convectional heating from the hybrids; the resulting higher temperature difference is quite accurately compensated by the lower temperature of the coolant at the end of the cooling pipe, as was shown in fig. 2c.

At a coolant temperature of –27 °C, the temperature differences for the middle and inner ring cooling pipes deviate only a few percent from those of figure A1. At higher operating temperatures, the temperature differences are smaller by roughly 1% for each 1 °C increase of the coolant temperature. This was demonstrated in fig. 3.

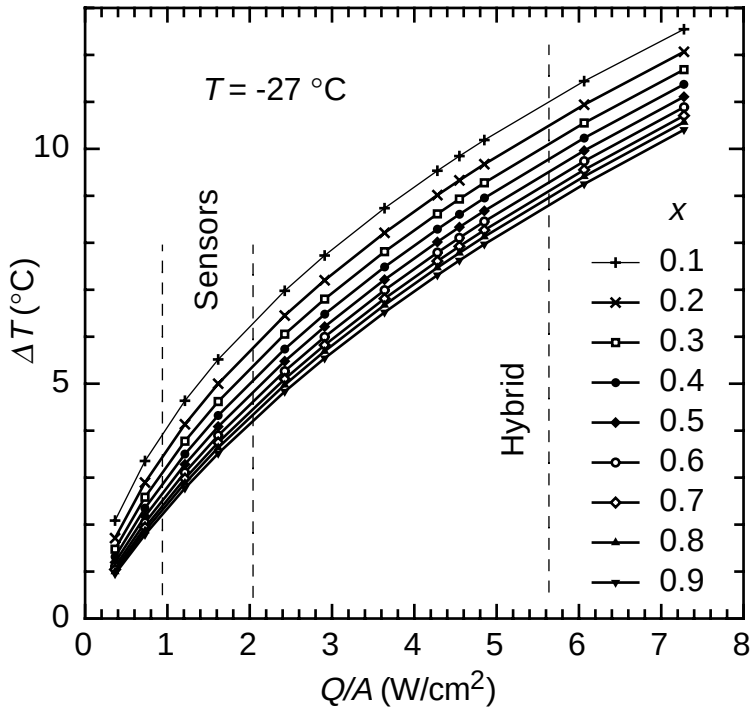

Figure A1: Dependence of the temperature difference between the pipe wall and the two-phase coolant C_3F_8 on the heat flux at –27 °C coolant temperature. The dashed vertical lines indicate the range of heat flux expected from the sensors and the maximum heat flux from the hybrid. The contact areas are 0.6 cm^2 for the sensors and 1.5 cm^2 for the hybrid.

Figure A1 shows that even at maximum heat flux from the sensors, the sensor cooling blocks are 4 to 5 °C colder than the hybrid cooling blocks. This demonstrates that splitting the cooling block results in stable operation at coolant temperatures that are about 4 °C higher than in the case that one block of similar mass would be used for cooling both hybrid and sensors.

A.I.6 Heat transfer in the ‘fin’ geometry

The design of split cooling blocks requires the evaluation of the thermal isolation between the two sides of the cooling block, attached to the same cooling pipe. The bypass of heat through the two-phase coolant is minimal, because the coolant is practically isothermal apart from a thin skin layer where the thermal gradient between the pipe wall and the bulk fluid resides. The conduction along the skin layer in the direction along the pipe surface can be ignored in first approximation. Ignoring also the heat transport by conduction and convection of the ambient gas, the conduction along the cooling pipe wall remains. This may thermally short-circuit the two blocks, unless some minimum requirements are satisfied. The problem is the same as that of thermal ‘fins’, which are used for improving the heat transfer in many heat exchanger structures.

Assume a cooling pipe with diameter *D* and wall thickness *t* going through a cooling block made of a material that has a high conductivity so that it is isothermal. The wall thickness *t* is so small that the heat conduction through the pipe wall causes a very small temperature drop in comparison with the temperature drop between the pipe wall and the coolant. The pipe wall has the same temperature as the inside surface of the block and then gradually descends towards that of the fluid. The heat conducted along the pipe wall is

$$\dot{Q}(z) = \kappa \pi D t \frac{dT(z)}{dz} \tag{A20}$$

where κ is the thermal conductivity of the pipe material (assumed constant within our range of temperatures), and $T(z)$ is the pipe wall temperature distribution along the direction of the flow. This is gradually decreased because of the heat transferred from the pipe wall to the coolant, given by the boiling flow heat transfer coefficient $h(T(z) - T_c)$ where T_c is the coolant temperature. We emphasise that this coefficient is not a constant but decreases slightly with smaller temperature difference (see section 4.3). The heat exchanged with the pipe wall and the coolant is

$$\frac{d\dot{Q}(z)}{\pi D dz} = h[T(z) - T_c][T(z) - T_c] \tag{A21}$$

If the boiling flow heat transfer coefficient is taken to be constant, the pair of differential equations (A20) and (A21) yields

$$T(z) - T_c = (T_b - T_c)\exp\left(-\frac{z}{\lambda}\right) \tag{A22}$$

where T_b is the block temperature and λ is the thermal decay length given by

$$\lambda = \sqrt{\frac{\kappa}{h} t} \tag{A23}$$

If the temperature dependence of the heat transfer coefficient is described by a function, the analytical solution of the equations is usually possible but does not yield much more insight in the problem. We may rather think that λ is slightly increased as one gets further from the block. However, this increase is quite insignificant in view of other uncertainties in our problem. We may therefore estimate *h* using its value at the block temperature.

The amount of heat conducted away from the block along the pipe is

$$\dot{Q}(0) = -\kappa \pi D t \frac{dT(z)_{z=0}}{dz} = \kappa \pi D t \frac{T_b - T_c}{\lambda} \tag{A24}$$

A thick cooling pipe of high-conductivity material could thus be used for improving the heat transfer between the fluid and the block, because an additional length of several pipe diameters could be used. Comparing with the heat exchanged with a block of length *L*, the improvement is

$$\frac{2\dot{Q}(0)}{\dot{Q}_b} = \frac{2\kappa\pi Dt\,\dfrac{T_b - T_c}{\lambda}}{h\pi DL(T_b - T_c)} = \frac{2\kappa t}{hL\lambda} = \frac{2\lambda}{L} \tag{A25}$$

The effect of thermal conduction along the cooling pipe wall can thus be taken into account by adding 2λ to the block length L.

If two blocks with high thermal conductivity separated by a gap d are attached to the thin-wall cooling pipe, the temperature distribution along the pipe wall in the gap depends on the ratio λ/d in a way which is illustrated in Fig. A2. In this case the block to the right of $z = d$ is warmer than the other which sits on the left of $z = 0$. When $\lambda = d$ some heat is conducted along the pipe wall from the hot block to the colder one, but when $\lambda = 0.5d$ the derivative of $T(z)$ becomes negative at $z = 0$ This indicates that the pipe appears rather as a thermal fin for both blocks. If λ/d is reduced further, the pipe wall temperature gets closer to that of the coolant, thus isolating the blocks better from each other. On the other hand, the amount of heat carried by the pipe section in the gap to the fluid becomes saturated, and therefore a very large gap will not improve the performance of a split block. A reasonable thermal separation of the two blocks is achieved at values close to $\lambda = 0.5d$ .In this case we may call the system a 'thermally split block'.

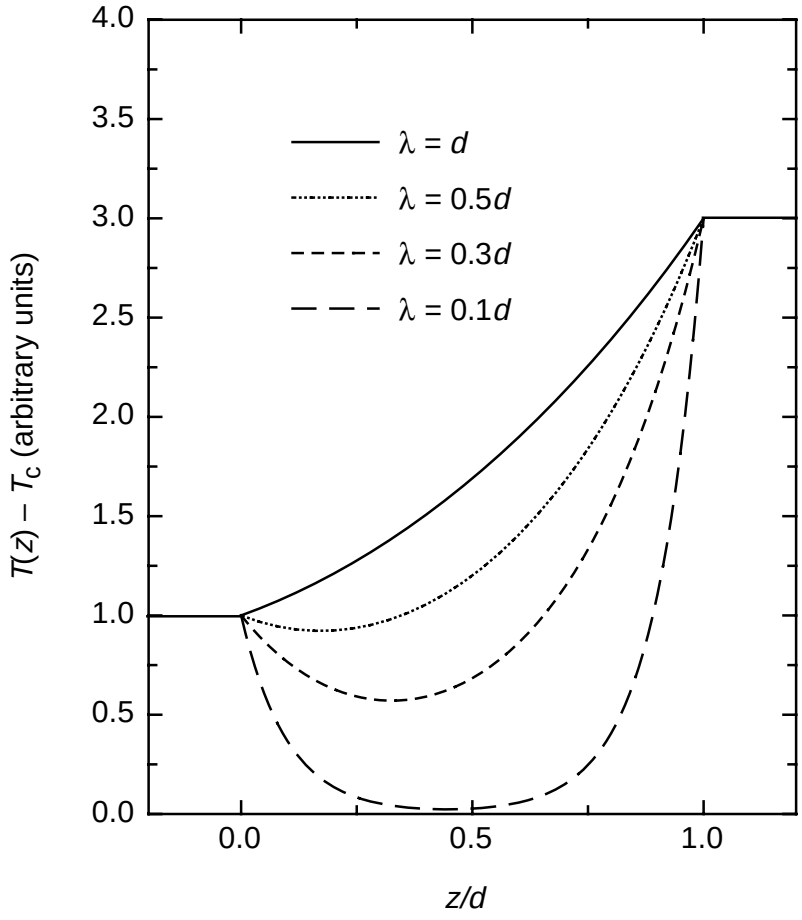

Figure A2: Temperature distribution of the pipe wall in the gap between the sides of a split cooling block. See the text for explanation.

The 50 µm thick CuNi cooling pipe has a conductivity of 0.294 $Wcm^{-1}K^{-1}$ and a fin length of 0.54 mm. For comparison, the aluminium alloy pipes of 0.2 mm thickness have a conductivity of about 2 $Wcm^{-1}K^{-1}$ and a fin length of 4.5 mm.

If the cooling blocks are attached to the CFC skin of the disk, the skin becomes a thermal fin, which absorbs convectional heat load from the hybrids and sensors. The skin thermal decay length in this case becomes

$$\lambda_{CFC} = \sqrt{\frac{\kappa_{CFC}}{h_c} t_{CFC}} \tag{A26}$$

where h_C is the convectional heat transfer coefficient discussed below. Extensive measurements have been performed on integrated cooling channels to determine the conductive properties of the skin [8].

A.I.7 Convectional heat transfer from hybrid to ambient and CFC skin

Assume that the end-tapping hybrid has on each side a hot area $A = W*H$ corresponding roughly to the width W of the horizontal row of ASICs times the height H of the hot area. Latter is the height of the ASICs. The rest of the hybrid forms a cooling fin, which we shall ignore for simplicity. This simplification is justified by tests and simulations, which show that the ASICs are at a temperature about 40 °C higher than that of the cooling block. However, most of the hybrid is only at about a 15 °C higher temperature.

The heat transfer from the ASICs on the side opposite to the wheel is by free convection, whereas on the side of the wheel the heat transfer is by convection in restricted space.

The free-convection heat transfer from the ASICs to the ambient gas is given by

$$\dot{Q}_c = h_c \Delta T A \tag{A27}$$

where the convection heat transfer coefficient h_c is given by

$$h_c = \kappa N_{Nu} H^{-1} \tag{A28}$$

The Nusselt number is

$$N_{Nu} = a\left(N_{Gr} N_{Pr}\right)^n \tag{A29}$$

and is obtained from the mean values of the Grashof and Prandtl numbers

$$N_{Gr} = \frac{\alpha g \Delta T \rho^2 H^3}{\eta}$$
$$N_{Pr} = \frac{\eta c_p}{\kappa} \tag{A30}$$

In the above expressions, α is the thermal expansion coefficient and is given simply by

$$\alpha = \frac{1}{\rho}\frac{d\rho}{dT} = \frac{1}{T} \tag{A31}$$

for an ideal gas such as nitrogen, g the gravitational acceleration, κ the thermal conductivity, ρ the density, c_p the specific heat, and η the viscosity of the convecting fluid. In our case, the ambient nitrogen gas is taken at the mean value of the temperature in the convecting gas layer. In practice, this mean value can be regarded as the average of the temperatures of the ASICs and the gas far away (free convection from the ASICs on the side opposite to the wheel) and the average between the ASIC and the CFC skin temperatures (convection in the restricted space).

Here, the parameter N_{Gr} is around 12000 and N_{Pr} = 0.731. Consequently, $N_{Gr}N_{Pr}$ will lie in the range between 500 and $2\cdot10^7$ where a = 0.54 and n = 1/4. These yield a heat loss from the ASICs on the free-convection side $\dot{Q}_c$ = 230 mW when ΔT = 40 °C and when the row of ASICs is horizontal.

The heat transfer in the restricted spacing d between the ASICs and the CFC skin of the wheel is given by

$$\dot{Q}_r = \varepsilon_c \kappa \Delta T \frac{A}{d} \tag{A32}$$

where ε_c is the heat conduction enhancement factor due to convection, given by

$$\begin{aligned} \varepsilon_c &= 1 && \text{for } N_{Gr}N_{Pr} \le 2000 \\ \varepsilon_c &= 0.18\left(N_{Gr}N_{Pr}\right)^{1/4} && \text{for } N_{Gr}N_{Pr} > 2000 \end{aligned} \tag{A33}$$

which yield ε_c = 1.74 and $\dot{Q}_r$ = 130 mW.

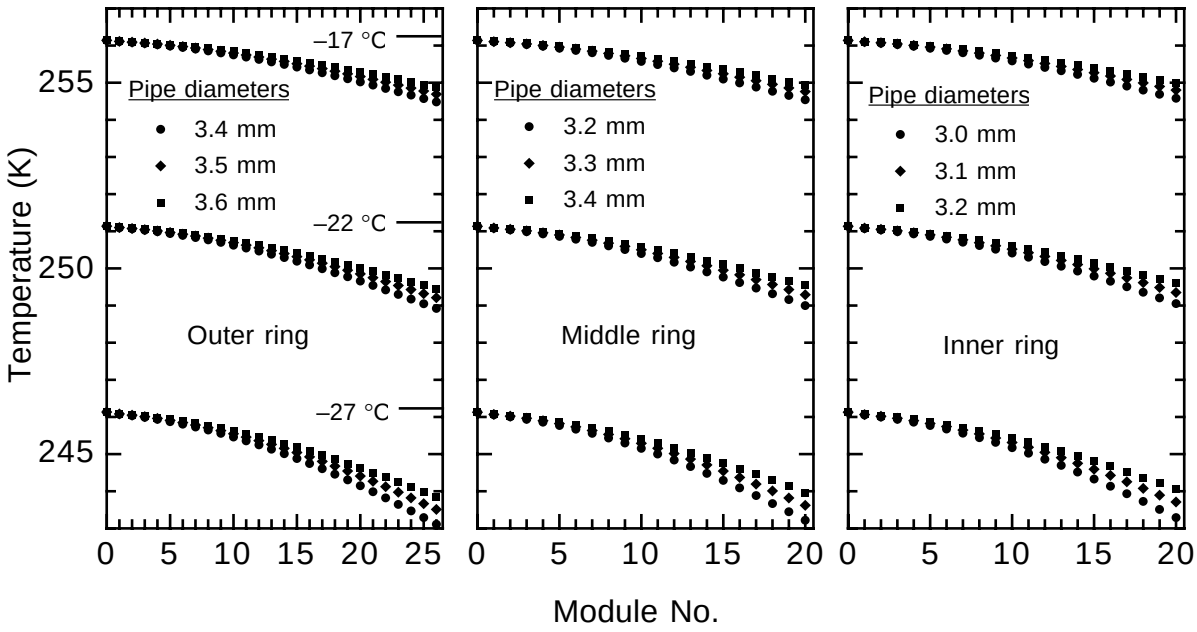

Figure A3: Coolant temperature at the cooling blocks of the outer, middle and inner ring modules for coolant input temperatures of –17 °C, –22 °C, and –27 °C. The pipe diameters are shown in the graphs.

The heat transfer in the restricted space is independent of the position of the module, whereas the free-convection heat transfer varies by $(H')^{-1/4}$ when the module position is rotated. Here H' is the vertical height of the hot surface and varies from H to W as the module is rotated. The free-convection heat loss to the ambient thus falls by 33% from horizontal to vertical position of the row of ASICs.

Ring	Pipe diam. (cm)	T_{in} (°C)	P_{in} (bar)	Δp (bar)	ΔT (°C)
Outer	0.34	-27	1.5434	0.1848	3.023
Outer	0.35	-27	1.5434	0.1616	**2.626**
Outer	0.36	-27	1.5434	0.1418	2.292
Outer	0.34	-22	1.8904	0.1619	2.217
Outer	0.35	-22	1.8904	0.1416	**1.929**
Outer	0.36	-22	1.8904	0.1242	1.686
Outer	0.34	-17	2.2970	0.1429	1.658
Outer	0.35	-17	2.2970	0.1250	**1.445**
Outer	0.36	-17	2.2970	0.1097	1.264
Middle	0.32	-27	1.5434	0.1783	2.905
Middle	0.33	-27	1.5434	0.1547	**2.504**
Middle	0.34	-27	1.5434	0.1348	2.170
Middle	0.32	-22	1.8904	0.1562	2.131
Middle	0.33	-22	1.8904	0.1355	**1.840**
Middle	0.34	-22	1.8904	0.1181	1.597
Middle	0.32	-17	2.2970	0.1379	1.594
Middle	0.33	-17	2.2970	0.1196	**1.379**
Middle	0.34	-17	2.2970	0.1043	1.198
Inner	0.30	-27	1.5434	0.1744	2.838
Inner	0.31	-27	1.5434	0.1499	**2.422**
Inner	0.32	-27	1.5434	0.1295	2.080
Inner	0.30	-22	1.8904	0.1527	2.082
Inner	0.31	-22	1.8904	0.1313	**1.781**
Inner	0.32	-22	1.8904	0.1134	1.532
Inner	0.30	-17	2.2970	0.1348	1.558
Inner	0.31	-17	2.2970	0.1159	**1.334**
Inner	0.32	-17	2.2970	0.1001	1.149

Table A2: Pressure and temperature drops for the cooling pipes on the three rings of modules for three input temperatures and three pipe diameters. The absolute pressure at the input is also given.

Appendix II: Alternative circumferential pipe design with equal pressure drops

The pressure gradient in two-phase flow of C_3F_8 was evaluated at the two design mass flow rates for three different pipe diameters, as a function of the molar fraction *x* of the vapour phase (the 'quality factor of the fluid), at three operating temperatures and for the three rings. The pressure gradient was integrated to yield the pressure at each cooling block, and this pressure was converted to fluid temperature using the equation for saturated vapour pressure, similar to what was presented in section 3.1. The chosen pipe diameters, pressure and temperature drops are summarised in table A2.

The temperature variation of the coolant along the outer, middle and inner ring cooling pipes is shown in figure A3.

On the basis of the above table, we have chosen the cooling pipe diameters of 3.5, 3.3 and 3.1 mm for the outer, middle and inner rings, respectively. Table A3 shows the maximum temperature drops at the three operating temperatures. These temperature drops are quite similar for all rings and are around 1.4 °C at –17 °C, 1.9 °C at –22 °C and 2.5 °C at –27 °C.

Ring	Pipe diam. (cm)	T_{in} (°C)	ΔT (°C)
Outer	0.35	-17	1.445
Middle	0.33	-17	1.379
Inner	0.31	-17	1.334
Outer	0.35	-22	1.929
Middle	0.33	-22	1.840
Inner	0.31	-22	1.781
Outer	0.35	-27	2.626
Middle	0.33	-27	2.504
Inner	0.31	-27	2.422

Table A3: The coolant temperature drops in the cooling pipes with diameters chosen so that roughly equal temperature drops are observed in all rings. Operating conditions are defined in table 2.

Appendix III: Safety factors and potential risks

Presently, the sensor power density after 10 years of operation has a safety factor of 4.5 for the most exposed inner-ring modules and a factor of 6 for the most exposed middle- and outer-ring modules. We discuss the additional safety factors, which result from our choice of worst-case parameters and potential risks that may have to be dealt with.

- Thermal conductivity of heat-path materials after irradiation:
  - the critical materials are TPG and C-C whose thermal conductivity does not deteriorate
  - ceramics, eutectic SnAg solder and CuNi do not deteriorate and none of them are critical to the design
  - the thermal conductivity of epoxies and silicon may deteriorate, but their thermal resistances are small in comparison with TPG and C-C due to geometry reasons. There is no risk to the thermal performance of the cooling system
- Manufacturing and assembly problems; design robustness:
  - the solder contact between the C-C block and the CuNi pipe may have areas that are unwetted by the solder on the side of the C-C composite. The wetting of CuNi, however, is excellent. If the unwetted spots have their smallest dimension more than the thermal fin length (0.54 mm), a deterioration of the effective heat transfer coefficient will result, proportional to the unwetted area. This can be revealed by metallographic examinations of the samples, and by thermal measurements. If the unwetted spot has one dimension of order of or less than the fin length, the deterioration of the effective heat transfer coefficient is minimal due to the high thermal conductivity of the C-C composite
  - the thermal performance of the solder contacts can be checked before assembly onto the disks by flowing mono-phase coolant through the pipe while pressing an array of heaters and thermometers onto the contact surfaces. Some 5 W of heating/contact suffices for detecting deviations from the expected performance, while the thermometers must have an accuracy of about 0.1 °C. The thermal contact of the heaters and thermometers is well assured by using a thermal gel adhesive sheet on their contact surfaces. These sheets are one side non-adhesive and non-staining, while they are available in various thicknesses from 250 µm up
  - grease contacts; these are non-critical but must, however, be checked. This might be best controlled by an infrared camera viewing the disk with mounted modules cooled at a fairly high temperature (~ 10 °C coolant temperature). The high coolant temperature is required because the unirradiated modules have a very small sensor power dissipation.
- Thermal modelling approximations:
  - most of the approximations made in our thermal simulations and calculations are pessimistic, i.e. their cumulative effect will improve the robustness of the design. The total power, for example, is assumed to be 8 W/module that is not derated at a lower coolant temperature. For example, operation at –27 °C coolant temperature, our lowest design value, yields the total power of 7.5 W/module with the outer ring modules irradiated to a fluence 6 times higher than 10 years of LHC operation. For these modules, at this temperature, thermal run-away is avoided with a safety factor of more than 12.
  - The heat transfer between the cooling block halves via the cooling pipe and the ambient gas is negligible in comparison with the heat transfer uncertainty via the fan-ins. Moreover, these thermal resistances were set to infinity in our thermal simulations. This is more than justified by

pessimistic approximations in the calculation of the effective thermal resistance of the fan-ins.

– The cooling of the disk by the blocks and pipes was not included in our simulations. Inclusion lowers the sensor temperature slightly and therefore improves their protection against thermal run-away. Similarly, the thermal contact of the sensors with the disk slightly improves the uniformity of the sensor temperature and also improves thermal stability. An important factor here is that the cooling pipe runs circumferentially *under* the modules and is located *underneath* the ASICs on the hybrid.
– The power supplies limit the sensor current and therefore prevent thermal run-away. The charge collection efficiency will suffer when this happens. This can only be avoided if the coolant temperature can be lowered sufficiently to compensate the higher leakage current. This is one of the reasons why we have designed the cooling system to operate down to –27 °C at the nominal full power available from the power supplies.

Appendix IV: Thermal run-away modelling of the modules

Figure A4 shows the components constituting the thermal circuit model used in our thermal run-away simulations. The average temperatures at the various component interfaces are calculated using Kirchoff's law for an analogous electric circuit, modelled in figure A5. Unlike an ordinary resistor network, our model includes non-linear elements symbolised by diodes. The correlation between heat flux and temperature difference in two-phase flow heat transfer as expressed in Eq. (5), resembles the behaviour of a junction diode.

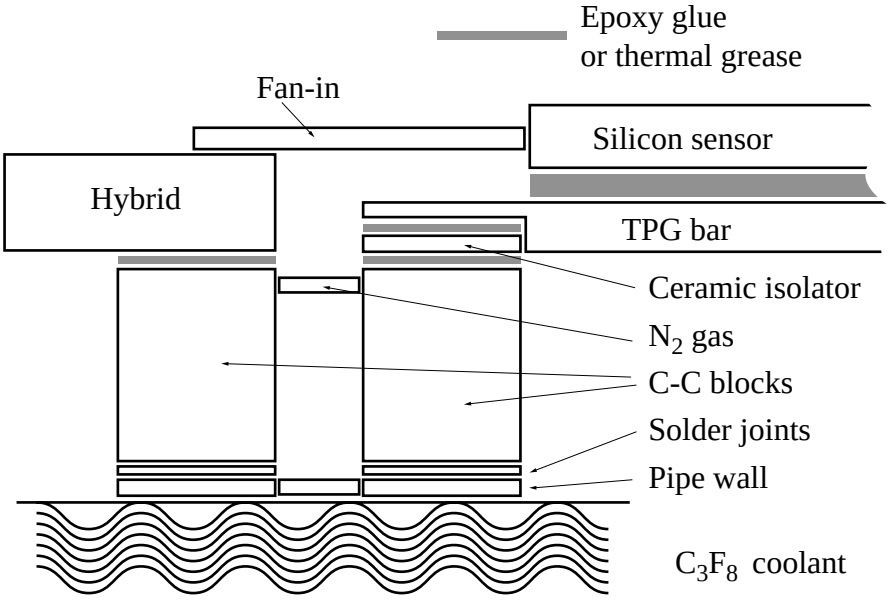

Figure A4: Components of the heat transfer path from the hybrid and sensors to the two-phase coolant in a silicon detector module.

The effective thermal resistances are defined as a difference of the temperatures on two interfaces

divided by the total heat flow passing through these interfaces. The temperatures are the average temperatures of the interface surfaces as obtained from the FE analysis. These resistances are not strictly constants, but deviate so little from a constant value that it is felt that they can be used for thermal run-away modelling. Moreover, their values are taken in stable conditions close to the run-away, so that the error due to possible non-linearity or poor definition is avoided.

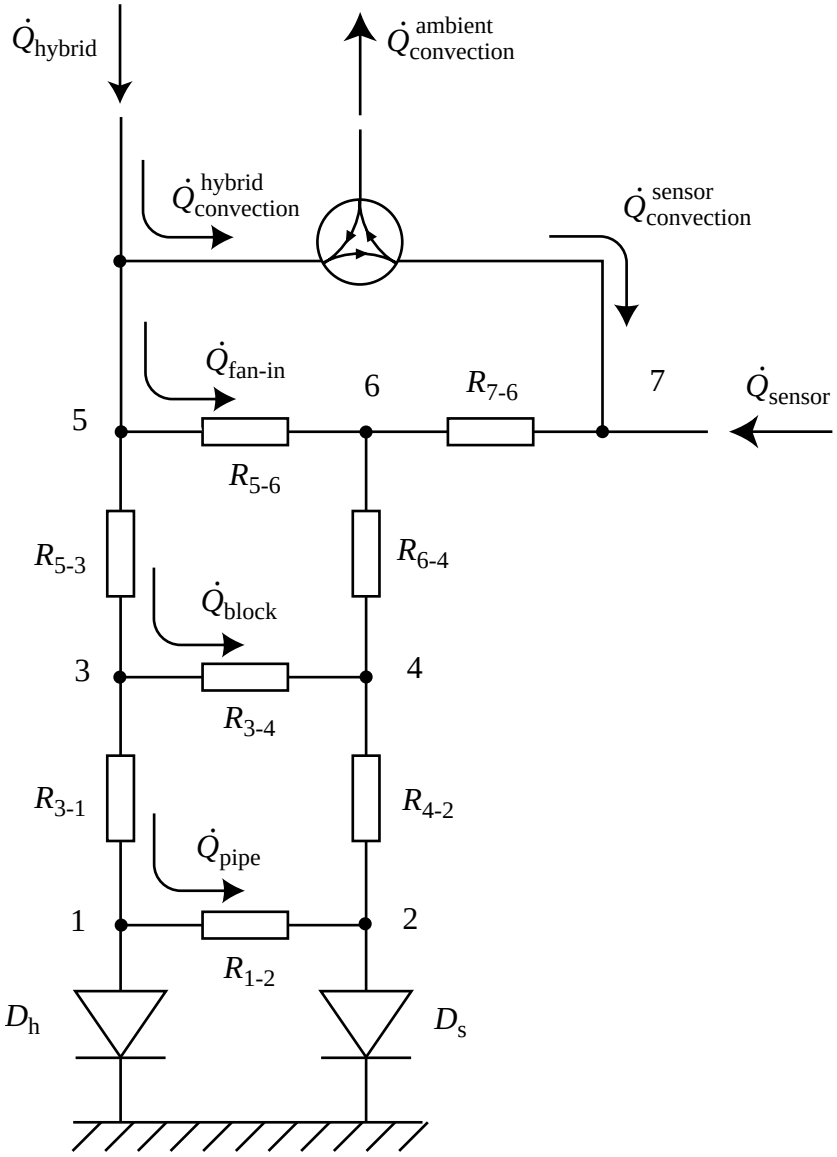

Figure A5: Electrical analogue model for the heat flow between heat sources (hybrid and sensors) and the coolant C_3F_8. The circulator allows to transfer an adjustable fraction of the convectional heat loss from the hybrid to the sensors, in order to simulate the various orientations of the module. The diodes model the non-linear heat transfer characteristics between the pipe wall and the two-phase coolant. The physical equivalence of the thermal resistors and diodes is shown in figure A4. Their values are given in the tables A4, A5 and A6, which detail the contributions to the resistance values.

The silicon temperature is defined as an average temperature that yields, see Eq. (1), the total power dissipated by the sensors in the FE calculation. This gives a weighted average temperature, which is closer to the maximum than to the minimum sensor temperature. Our electrical analogue model therefore gives a silicon temperature close to its local maximum value.

The individual thermal resistances can also be estimated from the geometry of the pieces and from their thermal conductivity, using the simple law

$$R_{eff} = \frac{L_{eff}}{A_{eff}\,\kappa} \tag{A34}$$

which assumes that the thermal conductivity is isotropic and does not significantly deviate from a constant value in the temperature range of interest and that the effective length and cross-sectional areas can be well defined in the range of power fluxes of interest. As only a few of these are well satisfied in our case, we have resorted to FE analysis for obtaining the effective thermal resistances and for verifying that they are constant in the relevant range of heat fluxes.

Hybrid heat path description (items)	Symbol in diagram	Baseline R_{eff} (K/W)	This work R_{eff} (K/W)
From fan-in edge to cooling contact		1.5	1.100
Grease contact		0.2	0.150
Total from hybrid edge to cooling block	$\boldsymbol{R_{5\text{-}3}}$	**1.7**	**1.250**
Hybrid block		0.3	0.320
Brazing or solder contact		?	0.004
Pipe wall		0	0.009
Total from top of block to pipe wall	$\boldsymbol{R_{3\text{-}1}}$	**0.3**	**0.333**
Heat transfer from pipe wall to C_3F_8	$\boldsymbol{D_h}$	**1**	**Eq. (4)**

Table A4: Effective thermal resistances for the hybrid cooling path used in our thermal run-away modelling. The estimated resistances of the Baseline design are shown for comparison. All numbers are derived using the heat conductivity of the materials and the geometrical shapes of the items in the path. The simulated temperature differences were compared with the FE calculations and were found to be in good agreement.

Because of non-linearity of heat transfer to the two-phase coolant and because of the non-linear relationship between the silicon temperature and power, the system cannot be solved by inverting a matrix of coefficients in a set of linear equations. Instead, the set of equations must be solved by nested iteration loops. This was carried out using the Excel™ spreadsheet programme. The programme was written so that both the silicon power density and the coolant temperature could be

varied until the run-away occurred. The run-away was detected as a point at which the solution of the equations diverged. The divergence occurred always very sharply even when using temperature steps of 0.05 K.

The nodes in the model of fig. A5 were chosen so that the effective couplings between the two heat paths could be reasonably modelled. This is very simple and reliable in our case because the isolation between the halves of the block is very good. The nodes in the hybrid path describe points at the edges of the hybrid (5), on top of the hybrid cooling block (3) and at the inner wall of the cooling pipe soldered to the hybrid block (1). In the sensor heat path the nodes are the silicon sensors (7), the end of the unthinned section of the TPG strip (6), the top of the sensor cooling block (4) and the inner wall of the cooling pipe soldered to the sensor block (2).

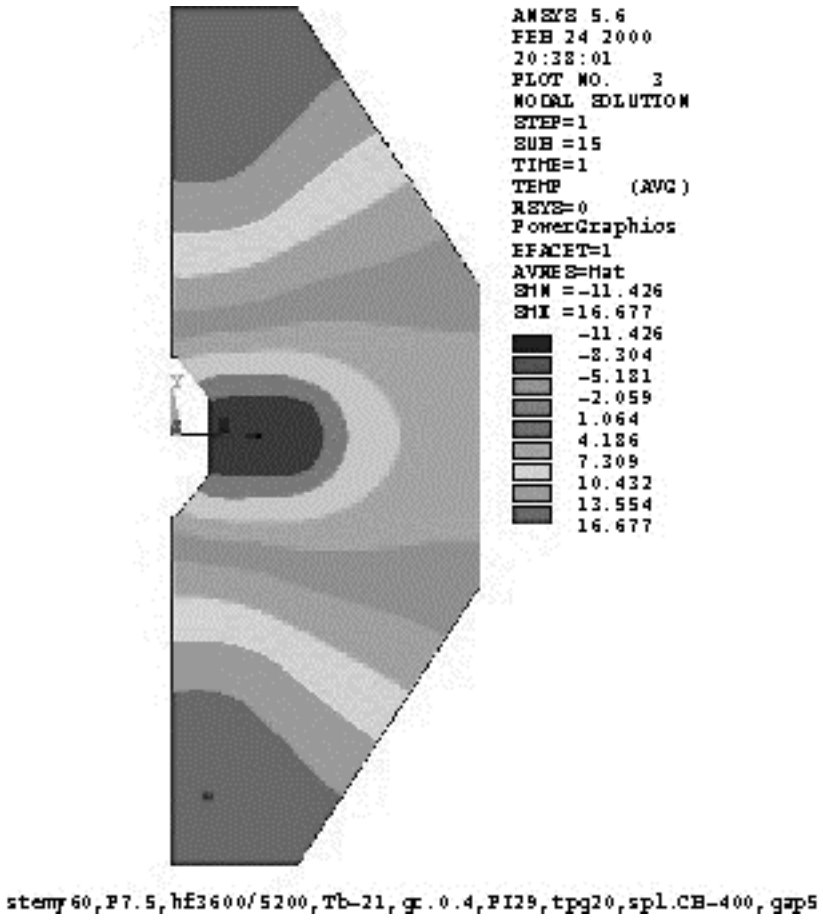

Figure A6: Temperature map of the hybrid substrate obtained using FE analysis at a coolant temperature of –21 °C. The maximum temperature of the hybrid edge is 16 °C, i.e. 37 °C above that of the coolant.

A fraction of the hybrid power was allowed to be dissipated by free convection into the ambient gas surrounding the detector. This power is roughly constant for all hybrids and amounts to ~ 230 mW. Convectional losses are mainly cooled by the sensors, which represent the largest cooled surface in the thermal system. However, not all sensors receive the same heat load because of the relative

positions of the hybrids and sensors in the various sectors of the wheels. The worst occurs at the top sector of the outer ring modules. Here, the sensors of a module may receive more than twice the convectional heat load. The resulting thermal imbalance is quite well compensated by the lower coolant temperature and higher heat transfer coefficient in the top sector, as was described in sections 3.1 and 4.3.

Table A4 shows the effective thermal resistances in the hybrid heat path. We have reached a minor improvement in comparison with the Baseline design, mainly due to the larger contact area between the hybrid and the block, and due to a better thermal design of the hybrid in this area. The details of the two designs were presented in figures 7 and 8. This improvement yields about 2 °C lower hybrid temperature, with identical block temperatures.

Figure A6 shows the thermal map of the hybrid substrate under conditions close to the thermal run-away of the sensors. The hybrid temperature defined in our model is the average temperature of the edge on which the fan-ins are glued. The heat loads through the fan-ins, obtained from the FE calculation on one hand and from our model on the other, agree with this definition. This is not surprising since the thermal conduction through the fan-ins behaves quite linearly due to the fact that on the sensor side the temperature is substantially lower and is much more uniform.

Table A5 gives the effective thermal resistances in the sensor cooling path. We notice significant differences between the two designs. Firstly, the resistance from silicon to the end of the TPG strip is much higher in our design. This is obvious because the whole length of the sensor area is cooled by the strip. Here, the effective thermal resistance of the Baseline design is a pure geometric result. The application of FEA would give a resistance close to zero since the sensors are almost exclusively cooled by the far-end block, even close to thermal run-away.

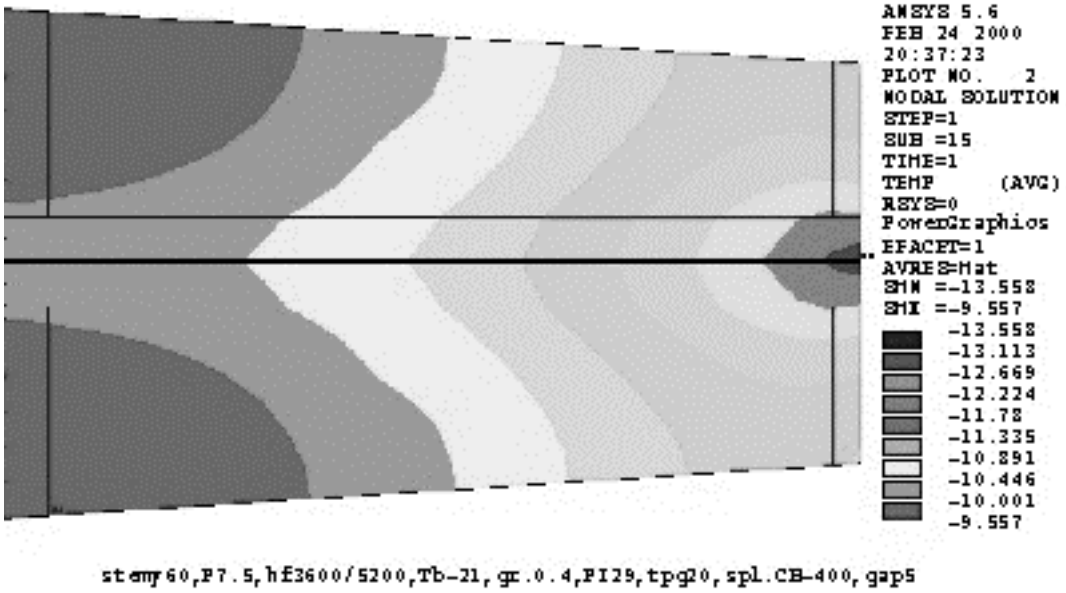

Figure A7: Thermal map of the sensors close to thermal run-away, obtained using FE analysis at a coolant temperature of –21 °C. The maximum temperature variation is less than 3.5 °C.

Sensor heat path description (items)	Symbol in fig. A5	Baseline R_{eff} (K/W)	This work (geom) R_{eff} (K/W)	This work (FEA) R_{eff} (K/W)
Silicon sensors			0.272	
Glue between silicon and TPG		0	0.050	
TPG		2	3.000	
Total from sensors to thinned TPG	$\boldsymbol{R_{7\text{-}6}}$	**2**	3.322[a]	**2.042**[b]
Thinned TPG		2.7	0.700	
Glue or grease		0.4	0.090	
Ceramic		0	0.060	
Thermal grease		0.3	0.370	
Total for contact area	$\boldsymbol{R_{6\text{-}4}}$	**5.4**	1.220[c]	**2.670**[d]
Sensor cooling block at hybrid end		0.5	0.400	
Brazing or solder		0	0.012	
Pipe wall		0	0.017	
Total from top of block to pipe wall	$\boldsymbol{R_{4\text{-}2}}$	**0.5**	**0.429**	
Heat transfer to C_3F_8	$\boldsymbol{D_s}$	**2.5**	**Eq. (4)**	
Silicon sensors (far-end)				
Glue between silicon and TPG (far-end)		0		
TPG (far-end)		1.5		
Thinned TPG (far-end)		1.8		
Glue or grease (far-end)		0.5		
Ceramic (far-end)		0		
Thermal grease (far-end)		0.2		
Sensor cooling block at far-end		0.5		
Brazing or solder (far-end)		0		
Pipe wall (far-end)		0		
Total from Si to far-end pipe inner wall	$\boldsymbol{R_{7\text{-}8}}$	**4.5**		
Heat transfer to C_3F_8 (sensor side)	$\boldsymbol{D_{s2}}$	**4**		

Table A5: Effective thermal resistances for the sensor cooling paths used in our thermal run-away modelling and simulation. The estimated resistances of the Baseline design are shown for comparison, including the far-end heat path. The numbers in the last column are obtained by FE calculation. All other values are obtained from the thermal conductivity and geometry of the items in the heat path. The values in bold characters were used in our simulations. — Notes: [a] This is the value giving the highest silicon temperature. [b] This FEA value gives the power-weighted silicon temperature used in our simulation. [c] This estimate based on the geometry is believed to correspond to the real thermal resistance of the contact area, but was not used in our simulation. [d] Estimate obtained from FE calculation is believed to be pessimistic, but was chosen for our simulations.

The thermal map of the sensors close to thermal run-away is shown in figure A7. The maximum sensor temperature is 11.5 °C above that of the coolant. Temperature maps, together with Eq. (1), were used for calculating the total power generated by the sensors. This power was then used for defining the average temperature of the sensors, again using Eq. (1), under the assumption that the temperature distribution is flat. The average temperature and the temperature at the end of the unthinned TPG bar together with the sensor power dissipation were then used to determine the effective thermal resistance $R_{7\text{-}6}$ in our model.

The FE method was also used for evaluating the effective thermal resistance $R_{6\text{-}4}$ of the contact area of the spine, from the end of the unthinned TPG bar to the top of the sensor cooling block. A substantial design improvement was achieved in comparison with the baseline spine. However, the resistance based on the FEA model is twice higher than given by a simple estimate and we believe that a more refined FEA model could further improve this resistance value. It was nevertheless chosen for our thermal run-away simulations.

Another large difference occurs close to the contact with the sensor cooling block. Here we have reached a very significant improvement by modest geometrical changes that take advantage of the high conductivity of the TPG. Further improvements may still be possible.

The thermal resistances of the blocks themselves are quite identical and are small in comparison with those in the contact area. In the baseline design, the blocks are glued onto the pipes. We have assumed that the resistance of the glue can be ignored which is unrealistic.

Thermal resistances between the hybrid and sensor cooling path nodes -excluding convection- (item)	Symbol in diagram	Baseline R_{eff} (K/W)	This work R_{eff} (K/W)
Fan-ins	$\boldsymbol{R_{5\text{-}6}}$	40	**263**
Material between the hybrid and sensor blocks	$\boldsymbol{R_{3\text{-}4}}$	2	**500**
Cooling pipe	$\boldsymbol{R_{1\text{-}2}}$	2	**>1000**

Table A6: Effective thermal resistances between the sensor and hybrid heat paths compared with their values in the Baseline design.

Table A6 shows the thermal resistances between the two sides of the of the split cooling block. Because our proposed design requires excellent cooling of the sensors via a single cooling point, isolation of the sensor side is important. The main coupling in our case is via the fan-ins, which link the hybrid and sensor edges. The block is completely split mechanically and its halves exchange heat only by conduction in the N_2 layer separating them; convectional heat transfer in the gap can safely be ignored. The cooling pipe wall is heat sinked to the coolant in the 1 mm gap separating the soldered areas. Therefore, the effect of the wall is to slightly extend the effective contact areas of the blocks, in particular that of the hybrid block. The effective resistance along the pipe wall in our design can therefore be assumed infinite.

Figure A8 shows the results of a typical thermal run-away simulation of the outer ring module, at the canonical value of the power density constant Q_o = 240 μW/mm^2. The temperatures of the nodes in the sensor heat path are plotted using filled symbols, and those of the hybrid heat path by open symbols.

It can be noted that at all coolant temperatures the dominant thermal resistance in the sensor heat path is between the nodes 6 and 4 which describes the region between the sensor block and the end of the unthinned TPG strip. As described above, this resistance was obtained from the FEA simulation and is higher than that obtained by simplified calculation. The temperature drop across the sensor block is less than 0.5 °C and it demonstrates the advantage of using the C-C composite with high thermal conductivity.

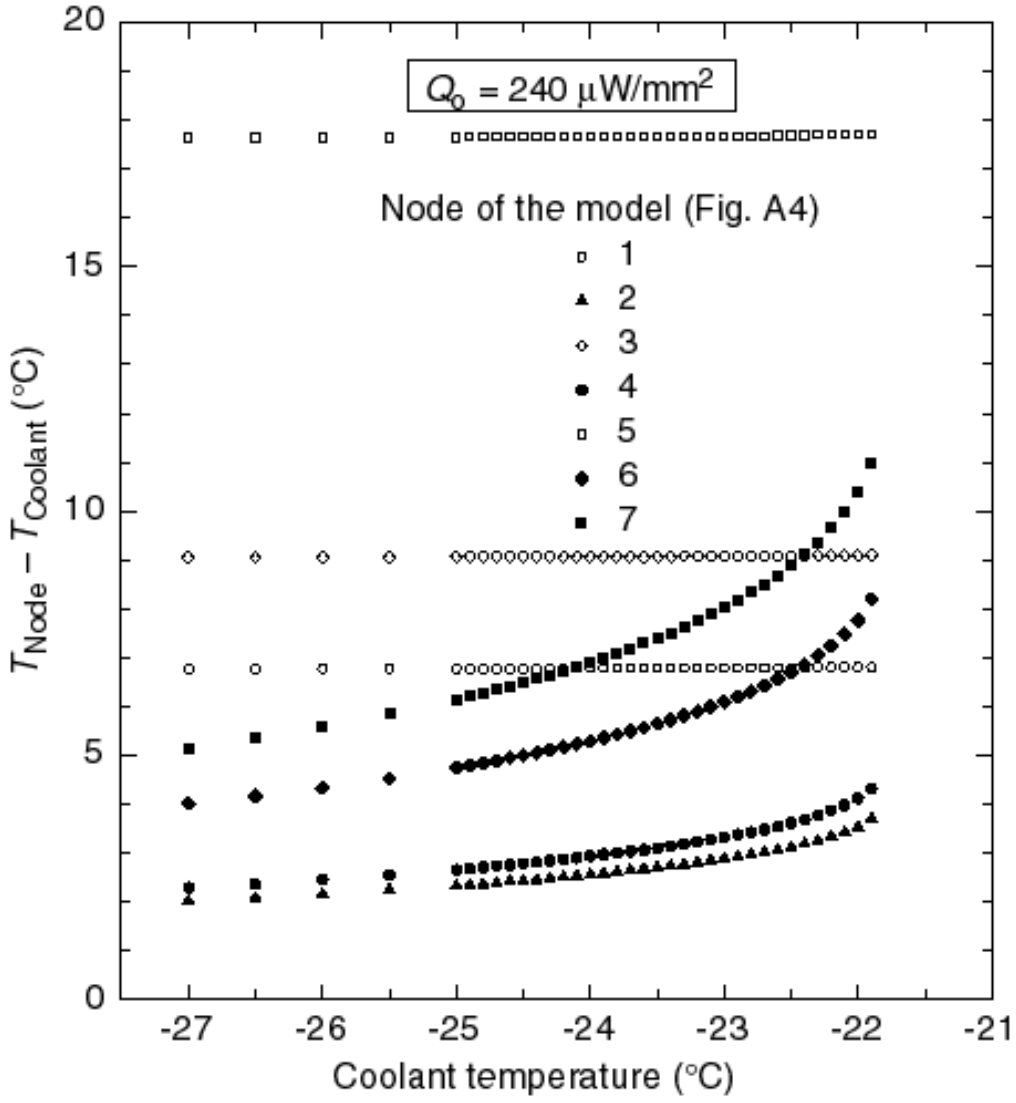

Figure A8: Temperature differences between the coolant and the various nodes of the thermal resistor model for the outer ring module described in the text. All resistances of fig. A5 are included in the model and their values are given in the tables A4, A5 and A6 in bold characters.

The large temperature difference between the nodes 3 and 4 demonstrate the effectiveness of the split between the cooling block sides. The temperatures of these nodes are those on the top of the hybrid and sensor blocks, respectively.

In the baseline design the aluminium blocks are mechanically not entirely split. Moreover, the aluminium cooling pipes short-circuit the two sides of the blocks. The result is that the semi-split aluminium blocks are practically isothermal. In other words, the semi-split is entirely ineffective.

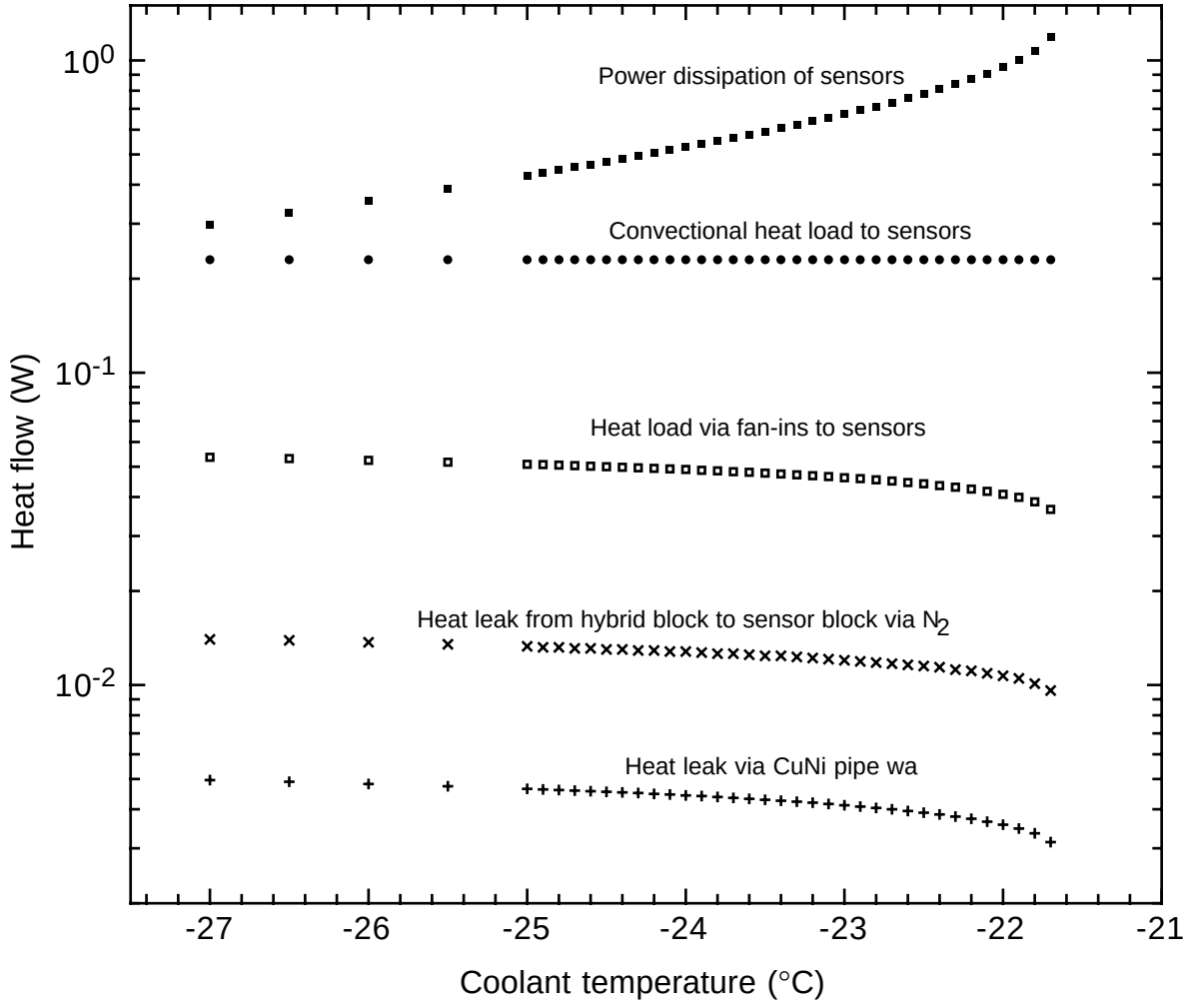

Figure A9: The power dissipation of the sensors, the convectional heat load and the heat flows from the hybrid side to the sensor side of the main heat paths via the fan-ins, via N_2 gas and via the CuNi cooling pipe with 50 µm wall thickness, shown as a function of the coolant temperature. The operating conditions are the same as in fig. A6, i.e. the sensor power density at 0 °C is 240 µW/mm^2, and the two-phase coolant is C_3F_8 with quality factor x = 0.50.

Figure A9 shows the heat flow (power) to the various nodes of the sensor path of our model described in fig. A5. We note that the sensor power dissipation dominates all other heat loads to their cooling path at the canonical sensor power density. At lower power densities the convectional heat

load from the hybrid may become dominant in those modules which are oriented so that there are convection currents reaching them, i.e. that there are hybrids located in the immediate proximity below the sensors. In our work, we have assumed that the convectional heat load to the sensors of a module is equal to the maximum free-convection loss of a hybrid with the row of ASICs in a horizontal position, estimated to be 230 mW (see Appendix A.I.7).

At higher coolant temperatures, the sensors have a higher temperature difference relative to the coolant. As the hybrid temperature has a much lower dependence on the sensor power, the temperature difference between the hybrid and sensors is reduced at higher temperatures. Consequently, the heat load from the hybrid to the sensors via the fan-ins is reduced. This is shown by the relevant curve in the middle of the plot in fig. A9.

Similar behaviour is also clearly shown by the two bottom curves that describe the heat leak between the two sides of the split block. These heat loads are almost negligible, but they are included in the model in order to study and optimise the geometry of the various optional designs.

We have not included the heat paths via the CFC skin of the disk in our model, although the heat conductivity of CFC is not negligible. The reasons for this are the following:

- The thermal coupling by the skin between the blocks sides is strongly reduced by the fact that the pipe wall between them is glued to the skin, providing an efficient heat sink which reduces the thermal cross-coupling.
- Moreover, the cooling pipe is also glued to the skin between the neighbouring split blocks, providing additional heat sinking of the skin.
- The heat load to the skin is reduced by the rather low convectional heat transfer between the hybrid and the skin on one hand, and between the sensors and the skin on the other. It is quite difficult to provide a reliable estimate of the temperature field of the skin under these conditions.
- The radiative heat load to the skin, probably dominating the radiative heat load to the sensors, only helps cooling the hybrid.
- The overall effect of the skin is to lower the temperatures of both sensors and hybrid by providing additional heat paths from the heat sources to the coolant.

The omission of the thermal effects of the CFC skin is thus a pessimistic approximation that improves the safety margins of our design. If more precise data on the heat transfer parameters would become available for the main heat paths, it may also be worth extending the model to include the effects of the CFC skin.

References

[1] T.O. Niinikoski, Evaporative cooling - Conceptual design for ATLAS SCT, CERN ATLAS Note ATL-INDET-98-214 (1998).

[2] E. Andersen, D. Bintinger et al. in: '5th Workshop on Electronics for LHC Experiments', Snowmass, Colorado (1999), Ed. C. Decosse (CERN LHCC Electronics Board). Proceedings available at: http://nicewww.cern.ch/~lebwshop/LEB99_Book/LEB99_Proceedings.html.

[3] C. Heusch, A. Holodenko and H.-G. Moser, Measurements of Silicon Detector Thermal Run-away, Max-Planc-Institut für Physik ATLAS INDET Note ATL-INDET-99-015 (1999).

[4] P.B. Whalley, Two-Phase Flow and Heat Transfer (Oxford University Press, Oxford 1996).

[5] R. Barron, Cryogenic systems (McGraw-Hill, New York 1966).

[6] The engineering drawings prepared by Jarl Buskop are available at Web address: http://www.nikhef.nl/pub/departments/mt/projects/atlas/sct/pictures/alternative_cooling/

[7] N. Brooks and B. Hawes, CTE of NIKHEF CFHC composite –Summary of ESPI measurements-, Oxford, 1999. We also wish to thank Armin Reichold for his assistance.

[8] P. Balm, Motivation and design of the ATLAS SCT cooling system, Master Thesis, University of Amsterdam (1999).